# Feasibility studies for open charm measurements with NA61/SHINE experiment at CERN-SPS

by

Yasir Ali

A DOCTORAL DISSERTATION
PERFORMED IN THE INSTITUTE OF PHYSICS
JAGIELLONIAN UNIVERSITY
KRAKOW
(POLAND)
SUBMITTED TO THE FACULTY OF PHYSICS,
ASTRONOMY
AND APPLIED COMPUTER SCIENCES OF THE
JAGIELLONIAN UNIVERSITY
2015

Thesis advisor: Dr hab. Paweł Staszel

Project coordinator: Prof. Dr hab. Paweł Moskal

This thesis is dedicated to my parents for their love, endless support and encouragement and to my beloved fiance

# ACKNOWLEDGEMENTS

I would like to gratefully and sincerely thank my supervisor Dr hab. Paweł Staszel for his guidance, support and most importantly, his help during my PhD studies at the Institute of Physics Jagieollonian University. His mentorship was paramount in providing a well rounded experience consistent with my long-term career goals. I would also like to thank all members of the NA61 Collaboration, especially Prof. Dr Marek Gazdzicki, Dr Peter Seyboth and all other colleagues who helped me from time to time. I am also grateful to Antoni Marcinek and Sebastian Kupny for their consistent suggestions during my project.

I would also like to thank Prof. Dr. Roman Płaneta for his assistance and guidance. Additionally, I would like to be grateful and say thanks to the coordinator of International PhD-studies programme Prof. Dr Paweł Moskal for his all time help and support in four years during my stay in Krakow.

Finally, and most importantly, I would like to say thanks to my parents. Their support, encouragement, quiet patience and unwavering love were undeniably the bedrock upon which my educational carrier has been built. Their faith in me and allowing me to be as ambitious as I wanted. Thank you mom and dad. Also I am grateful to my fiance as she fully supported me while I stayed away from my home. It is quite difficult to find words to acknowledge everyone, who has contributed in one way or another to this thesis.

# LIST OF FIGURES

**Figure**

# LIST OF TABLES

**Table**

# ABSTRACT

A feasibility study for the $D^0$ meson (Open charm) measurements by its decay into two daughter particles, $D^0 \rightarrow K^-$ and $\pi^+$, in central Pb+Pb collisions and Ar+Ar collisions at SPS energies is presented. The study of open charm mesons which carries important information about the initial stages of the nucleus-nucleus collision at relativistic energies, will be a powerful tool to investigate the properties of the hot and dense matter produced in such collisions. To generate the physical input we use AMPT (A MultiPhase Transport model) event generator. We employed GEANT4 to describe particle transport through the experimental setup. The study is done assuming NA61/SHINE experimental setup supplemented with a future vertex detector that allows for precise vertex reconstruction in the target proximity. This detector will be used ultimately to measure open charm mesons in nucleus-nucleus collisions at energies accessible at CERN-SPS. The simulation results shows that the measurements are feasible. This thesis discusses the results obtained, based on the predicted yields of $D^0$ mesons. It also addresses the issue of vertex detector optimization, with the emphasis on the prospect of the development of a vertex detector based on CMOS technology.

# TABLE OF CONTENTS

# CHAPTER I

# Introduction

The physics of ultra-relativistic heavy ion collisions connects nuclear physics with high energy physics of elementary particles. Ultrarelativistic energies refer to the energy regime where the kinetic energy exceeds the rest energy significantly and the term "heavy-ions " refers to heavy atomic nuclei. Nuclear physics deals with complicated objects like nuclei while on the other hand high energy particle physics is mainly concerned with more elementary particles like leptons and quarks.

Collisions of subatomic particles at relativistic energies allow us to study the properties of hot and dense nuclear or hadronic matter in terms of elementary interactions. Quantum Chromodynamics (QCD) is the theory of strong interactions which fundamentally describes hadronic matter. Hadrons exists in two forms known as baryons and mesons. Baryons are made up of three quarks while mesons consist of a quark antiquark pair. It is believed that shortly after the Big-Bang, at the beginning of the Universe the matter was dominated by deconfined quarks and gluons that formed a medium known as the Quark Gluon Plasma (QGP).

There are two important features of QCD, namely asymptotic freedom and color confinement. Asymptotic freedom is the property according to which the attraction between quarks is weak at short distances and as the quarks are separated, the attraction becomes stronger. Asymptotic freedom in QCD was discovered by Gross,

Politzer and Wilczek [2, 3]. It allows precise predictions for high energy physics experiments in the hard-scattering regime based on the perturbative quantum field theory framework [4]. Colour confinement [5] is another striking feature of QCD. According to this phenomenon, quarks and gluons can not be directly observed due to their colour charge and are always bound within hadrons.

QCD predicts a phase transition between hadronic matter and partonic matter. This partonic matter of strongly interacting nature forms above the so called critical density. One of the earliest reviews, presented by Shuryak in 1980 [6], stated that "When the energy density exceeds some critical value of ($\approx 1\,\mathrm{GeV/fm^3}$), matter no longer exists in the form of hadrons (protons, neutrons, etc.) but of their fundamental constituents, quarks and gluons". Numerical calculations of QCD (Lattice QCD) predicts a phase transition temperature of approximately 170 MeV (1 MeV $\approx$ 1.1604 $\times\ 10^{10}$K) (at baryon chemical potential $\mu_B = 0$) [7] known as the critical temperature $T_c$. Quantitative predictions of Lattice QCD calculations [8] at zero net baryon density ($\mu_B = 0$) find that the phase transition is a rapid crossover.

At higher temperatures and baryon densities, the hadrons in ordinary matter melt into their constituent quarks and gluons which can move freely and form a new phase, the QGP. Figure 1.1 shows the nuclear matter phase diagram of temperature (T) versus baryon chemical potential ($\mu_B$) illustrating the different phases of strongly interacting matter.

Heavy-ion experiments at the Relativistic Heavy Ion Collider (RHIC) and the Large Hadron Collider (LHC) study strongly interacting matter at extremely high temperatures and low values of the net baryon density (i.e. small values of $\mu_B$). In this region of the phase diagram, QCD predicts the transition to be a smooth crossover from hadronic to partonic matter. Lattice QCD calculations and analytical calculations suggest a critical point at larger $\mu_B$. Beyond the critical point, one expects a first order phase transition from hadronic to partonic matter in the regime

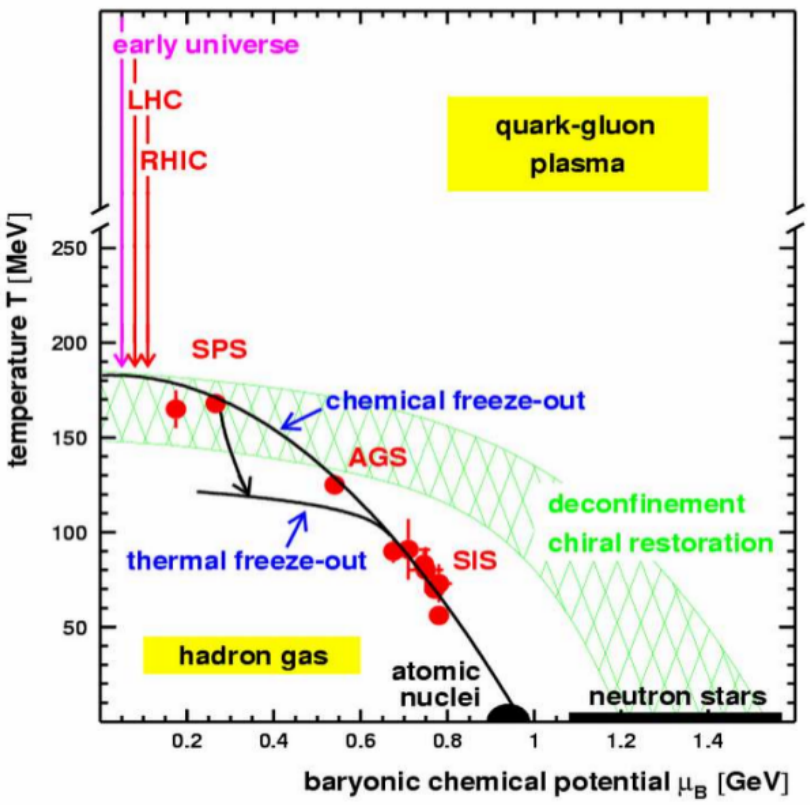


Figure 1.1: Sketch of the Phase diagram, of strongly interacting matter as a function of temperature and baryochemical potential [1]. Thermal model analyses of heavy ion collision data at AGS, SIS and SPS energies provide the hadrochemical freeze-out points (dots).

of higher $\mu_B$ and lower temperatures. The phase transition region is depicted as the light green coloured band. The solid curve along the freeze-out points in Figure 1.1 represents the parameterisation from a statistical hadron gas model with constant baryon density $\rho_B = 0.75\,\rho_0$ [1]. The freeze-out points are obtained by a statistical model analysis from particle ratios measured in heavy ion collisions [9, 10, 11]. It can be seen from the figure that the matter with extremely high $\mu_B$ and relatively low temperature exist inside the neutron stars.

Relativistic heavy ion collisions provide a unique opportunity to create strongly interacting matter at high temperature and density. Such hot objects are often called "fireballs ". The space-time evolution of the fireball created in high energy collisions is shown in Figure 1.2. This figure shows two different scenarios which depend on

the collision energy. The left-hand side of the figure shows a purely hadronic scenario where the energy density is not sufficiently high for the formation of QGP. On the right-hand side, the scenario with the creation of QGP is shown. In the QGP formation scenario there is a pre-equilibrium phase of $\tau \approx 1\,\mathrm{fm/c}$ (time given in the local frame) during which the produced partons rescatter both elastically and inelastically. After some time a local thermal equilibrium is obtained, leading to the formation of QGP (the red region in the figure). As the QGP expands collectively and cools down to a temperature around the critical value $T_c$, the hadronization takes place, a process in which hadrons are formed from the quarks and gluons. During hadronization, the system passes through a mixed phase composed of deconfined quarks and hadrons (represented by the yellow shaded band) before the complete transformation to a hadron gas is achieved.

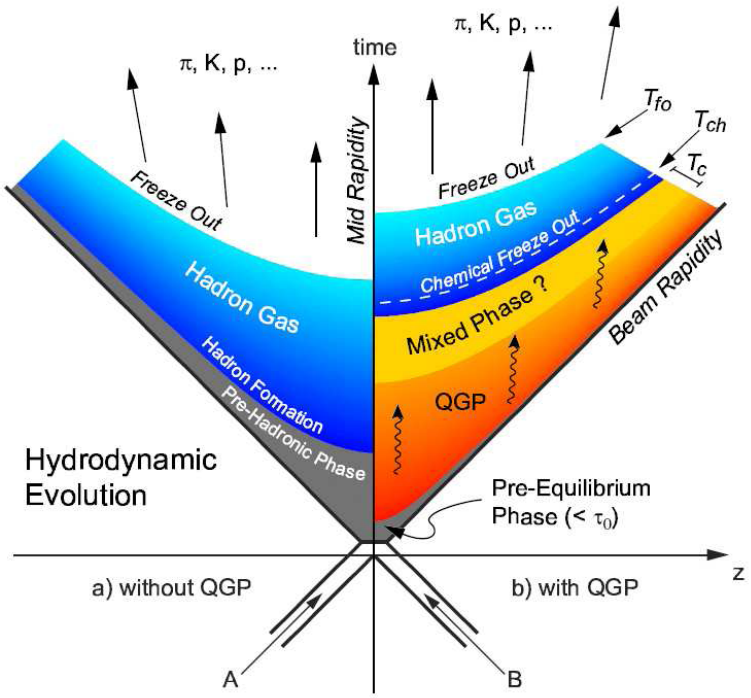


Figure 1.2: Representation of the space-time evolution of the fireball [12]. The purely hadronic scenario (i.e. no QGP formation) is depicted on the left-hand side while the right-hand side illustrates the expected evolution of the system including QGP formation.

In the conventional picture, the hadrons interact inelastically in the hadronic stage until the chemical freeze-out is reached when the system's inelastic collisions cease. After the chemical freeze-out, the energy of the rescattered hadrons is not high enough to change the yields of the different species. The system then continues to evolve through elastic collisions until a stage called kinetic (or thermal) freeze-out is reached. This occurs when the relative distance between particles is larger than the range of the interaction, so that elastic collisions among them cease. At this stage, the kinematic properties of the hadrons, in particular their momentum distributions, become fixed. Therefore, the transverse momentum spectra of the emitted particles reflect the conditions of the thermal freeze-out. The system breaks up into free hadrons that travel to the detection system. In this framework, the chemical and thermal freeze-out take place at two different instants in time.

Another model termed as single freeze-out model, also known as Cracow model, assumes that the chemical freeze-out and the thermal freeze-out occur simultaneously. This means that hadrons decouple completely when the thermodynamic parameters reach the freeze-out condition and thus no particle rescattering is present after the freeze-out. The resulting thermal distributions are then folded with a suitably parametrized hydrodynamic expansion, which involves transverse and longitudinal flow. The decay of resonances, including cascades, are incorporated in the Cracow model [13, 14].

Relativistic heavy ion collisions enable the creation of hot and dense strongly interacting matter over a wide range of temperatures and densities in a controlled laboratory environment [15]. Thus these collisions allow us to explore a stage of the early universe which was dominated by QCD matter. According to the standard cosmological model [16], the universe went through an inflation followed by a reheating period before entering a cooling process. At time t $\approx 10^{-12}$ s after the Big-Bang the electroweak phase transition took place as temperature dropped to the scale

of 100 GeV. Then at t $\approx 10^{-6}$ s after the Big-Bang, the universe reached to the temperature on the order of 100 MeV. At this temperature, the QCD phase transition occurred and quarks became confined in hadrons [17].

The available energies for relativistic heavy ion collision rapidly increased with the development of new accelerators i.e. from $\sqrt{s_{NN}} \approx 2.3$ GeV at the Bevalac experiment, $\sqrt{s_{NN}} = 5$ GeV at the Alternating Gradient Synchrotron (AGS), $\sqrt{s_{NN}} = 17.3$ GeV at Super Proton Synchrotron (SPS) to the Relativistic Heavy Ion collider (RHIC) which accelerated fully stripped Au ions to a collision energy of $\sqrt{s_{NN}} = 200$ GeV. Presently, the Large Hadron Collider (LHC) at CERN reaches the highest collision energies providing Pb on Pb reactions from $\sqrt{s_{NN}} = 2.76$ TeV to $\sqrt{s_{NN}} = 5.5$ TeV [18, 19]. The goals of heavy ion collision experiments are to study the QGP and more generally the phase diagram of strongly interacting matter. Present experiments can scan a large area of the phase diagram (refer to Figure 1.1), by varying the center-of-mass energies $\sqrt{s_{NN}}$ of colliding nuclei. In addition, the system size is also an important parameter that can be controlled experimentally and allows for further systematic exploration of the phase diagram. The experimental programs at the LHC facility [20] and the RHIC facility [21, 22, 23] have provided conclusive evidence of the formation of a deconfined state of matter in heavy-ion collisions where the quarks and gluons are the relevant degrees of freedom. Already at SPS energies, several observables are predicted, including phenomena like strangeness enhancement and $J/\psi$ suppression, which can be interpreted as signatures of the QGP phase transition [24, 25, 26]. In order to establish the energy dependence of rare processes such as production of $D$ mesons and multi-strange hyperons, it is necessary to perform high statistics measurements of Pb+Pb collisions at SPS energies. Indeed it is widely recognized that the measurement of mesons containing heavy flavour is of great importance for a better understanding of nucleus-nucleus reactions at relativistic energies [27].

This thesis presents the results of a feasibility study for the measurements of $D^0$ meson (open charm) production by its decay into two daughter particles, $D^0 \rightarrow K^- + \pi^+$, in central Pb+Pb collisions at the top SPS energy of 158A GeV and a lower energy of 40A GeV as well as in the lighter Ar+Ar system at 158A GeV. For simulation of the reactions, we used the AMPT (A Multi-Phase Transport Model) event generator. We employed the GEANT4 application to describe particle transport through the experimental setup. The actual measurement is planned within the NA61/SHINE experiment [28], which is a fixed-target experiment at the CERN SPS. The simulation results show that open charm measurements are feasible if the current NA61/SHINE detector is supplemented with a future Vertex Detector which allows for a precise track reconstruction in the proximity of the target.

Chapter 2 describes the physics motivation behind the open charm measurements. Chapter 3 comprises a description of the existing NA61/SHINE experimental setup at the CERN-SPS. In Chapter 4 we describe in detail the simulation framework and the reconstruction procedure for $D^0$ mesons. Chapter 5 presents the Vertex Detector technology, the detector response model and cluster simulation. Chapter 6 describes the results and discussion and finally Chapter 7 concludes the whole thesis.

This thesis is supplemented with an appendix which describes radiation damage in silicon detectors.

# CHAPTER II

# Physics motivation

In high-energy heavy ion collisions charm production is one of the important topics of theoretical as well as experimental research. It is widely recognised that the measurements of mesons containing heavy flavour help to better understand nucleus-nucleus reactions at relativistic energies. Due to the large mass, charm quarks are produced mainly at the early stage of relativistic heavy ion collisions and remain conserved during the fireball evolution [29].

The perturbative QCD (pQCD) based approach has been used for the interpretation of open and hidden charm experimental data [30]. This approach is based on the assumption that pQCD can describe charm production in elementary nuclear and hadronic collisions and that charmonium creation is due to the binding interaction between $c\bar{c}$ quarks. In nucleon-nucleus (p+A) and nucleus-nucleus (A+A) reactions a created charmonium state encounters subsequently interacts with the surrounding matter [31]. The standard approach assumes that a perturbatively produced charm quark forms a bound state with a lighter quark (d, u or s) for open charm production [32]. It was pointed out that available precise results on charmonium yields in p+A collisions are difficult to understand within the standard approach [33]. In 1997 Gorenstein and Gazdzicki [34, 35] observed that the $J/\psi$ yield in A+A collisions is proportional to the pion multiplicity and that the data may be explained by sta-

tistical production of $J/\psi$ at the hadronization stage. The statistical approach was also applied to open charm production, and it assumed that charmed quarks and anti-quarks are generated in the partonic phase according to the available partonic phase space. As in the standard approach, statistically produced charm quarks bind to light quarks to form charmed hadrons. The pQCD based and statistical estimates of open charm yields for central Pb+Pb collisions at 158A GeV differ by a factor of about 30 [34]. The predicted system size dependence in these two approaches is also very different.

Figure 2.1 shows the measured yield of $J/\psi$ production in In+In and Pb+Pb collisions at $\sqrt{s_{NN}} = 158\,\mathrm{GeV}$ as a function of centrality which is represented by the number of participating nucleons $\mathrm{N}_{part}$, scaled to pQCD predictions assuming normal nuclear absorption in the medium. It is observed that the yield is consistent with pQCD at the lower number of participants, however there is a significant drop of the ratio above $\mathrm{N}_{part} \approx 200$. This effect is known as anomalous $J/\psi$ suppression. This suppression reaches $\approx$ 20-30% for central Pb-Pb collisions. This phenomenon was initially related to the onset of QGP formation in the high density phase of nucleus-nucleus collisions (for details see Ref. [36]). However, other possibilities like interactions with co-moving hadrons can not be ruled out by this data [37, 38].

Further confirmation of the QGP formation hypothesis requires more charm production data. The multiplicities of various mesons in central Au+Au collisions from AGS to RHIC energies [27] as predicted by the Hadronic String Dynamic (HSD) model are depicted in Figure 2.2. The predictions are based on the charm production cross sections fitted to the experimental p+N and $\pi$+N data assuming that the total charm production in A+A reactions scales with the total number of nucleon-nucleon collisions [39]. It is seen that the open charmed hadron yields are much higher than the yields of the $J/\psi$ mesons particularly below the top SPS energy. Thus it is feasible and intended to measure open charm production both at maximum and medium

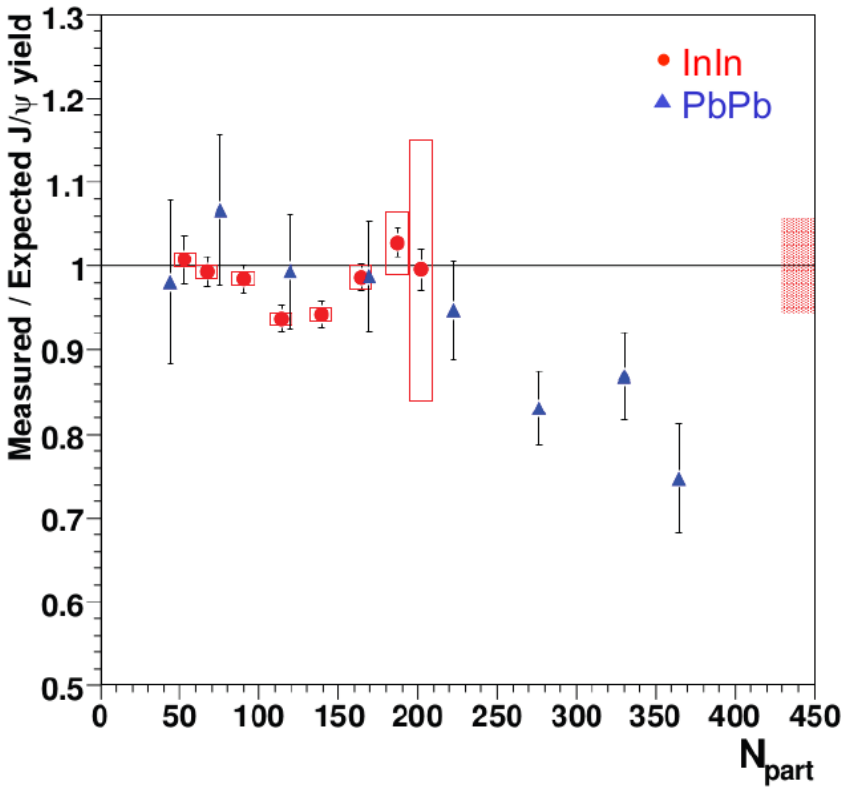


Figure 2.1: $J/\psi$ suppression pattern measured in In+In (dots) and Pb+Pb (triangles) collisions, as a function of the number of participants $N_{part}$ [40]. The boxes around the In-In points represent correlated systematic errors. The shaded box on the right shows the uncertainty in the absolute normalisation of the $J/\psi$ yields for the In-In interactions.

CERN-SPS energies in experiment NA61/SHINE (Super proton synchrotron Heavy Ion and Neutrino Experiment).

In the context of the phase transition between normal hadronic matter and the QGP, the charm-quark degrees of freedom are of special interest [39, 41]. It was predicted that $c\bar{c}$ meson states should no longer be formed in the coloured QGP medium due to colour screening [31, 42]. Indeed the measurement of $J/\psi$ mesons by the NA38/NA50 and NA60 experiments found a suppression in Pb+Pb collisions measured at the top SPS energy. On the other hand, the measurements of di-muon production provide hints of an enhancement of charmed meson production.

The NA50 experiment published data on di-muon production in p+A collisions

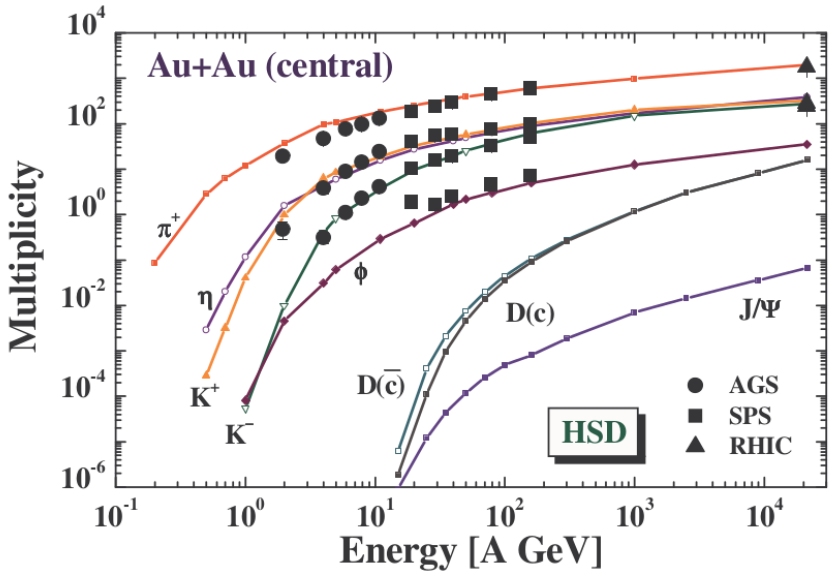


Figure 2.2: Collisions energy dependence of the multiplicities of $\pi$, $\eta$, $\phi$, $K^+$, $K^-$, $D$, $\overline{D}$ and $J/\psi$ in central Au+Au collisions predicted by the Hadron String Dynamics (HSD) model. This figure is taken from [27].

at 450 GeV/$c$ and Pb+Pb collisions at 158A GeV/$c$ in 2001. The p+A results are well described in terms of known sources like Drell-Yan processes and semi-leptonic decays of charmed mesons. However, an enhancement of pair production in the invariant mass region between $\phi$ and $J/\psi$ meson masses was observed in A+A data.

Figure 2.3 depicts the linear increase of the enhancement with the number of participants. The enhancement reaches a value on the order of three for central Pb-Pb collisions compared to the proton induced reactions. This increase may be related to enhanced production of charmed hadrons but alternative scenarios can not be ruled out by this data [43]

The NA60 collaboration published data on di-muon production in In+In collisions at the top SPS energy [44]. They confirmed the di-muon enhancement in the invariant mass range between the $\phi$ mass and $J/\psi$ mass first seen by the NA50 collaboration [43]. As mentioned above, the effect was tentatively attributed to an enhancement of open charmed meson production. The detailed analysis of the statistically more accu-

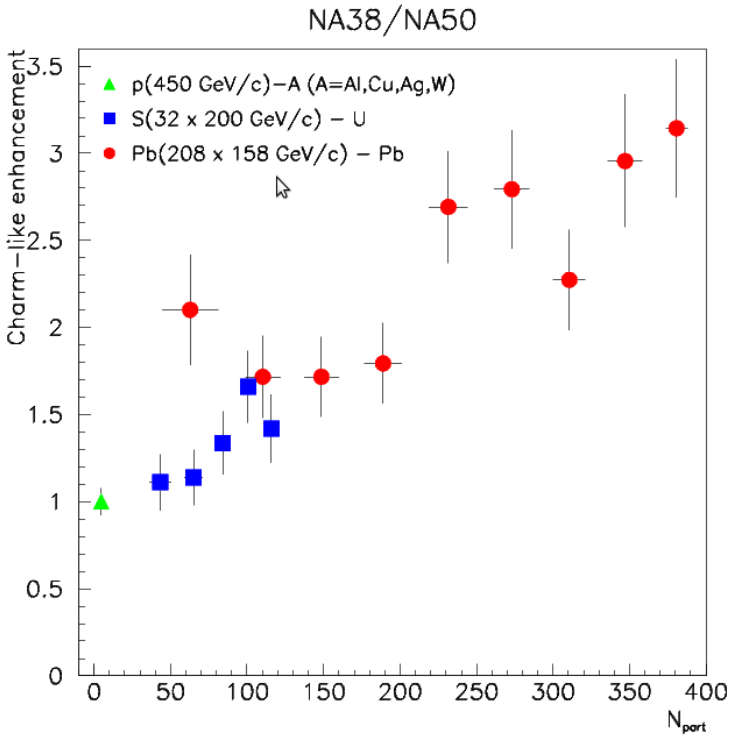


Figure 2.3: Di-muon enhancement in nucleus-nucleus collisions plotted as a function of the number of participants $N_{part}$. The enhancement (relative to nucleon-nucleon collisions) increases linearly with $N_{part}$ [43].

rate spectra from the NA60 collaboration showed that the enhanced component had an effective temperature $T_{eff}$ which increases continuously with increasing invariant mass in the range below $1\,\mathrm{GeV}/c^2$ followed by a relatively sudden drop (of 50 MeV) for masses above $1\,\mathrm{GeV}/c^2$ (see Figure.2.4).

The observed increase of the effective temperature ($T_{eff}$) in the lower mass region can be attributed to hadronic sources coupled to the expanding medium, however, it is hard to associate the observed $T_{eff}$ above 1 GeV to any known standard sources like Drell-Yan production or/and open charm fusion (see Figure 2.4). The NA60 collaboration proposed an interpretation in terms of creation of a muon radiation source at the early collision phase which they attributed to QGP [44]. This interpretation is based strongly on the D mesons production limits deduced from the di-muon data in a model dependent way. These limits can/should be verified by direct measurement

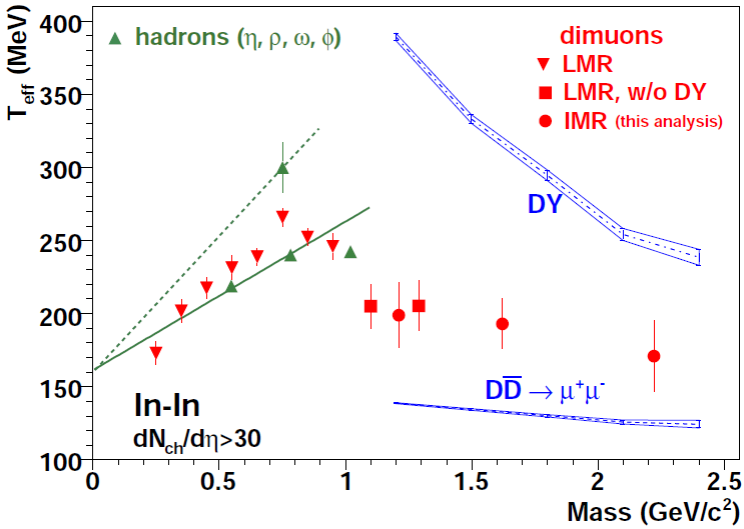


Figure 2.4: Inverse slope parameter $T_{eff}$ of the excess mT spectra vs dimuon mass. The bands show the inverse slopes for the Drell-Yan and open charm contributions as provided by the simulation code Pythia. Drell-Yan is not subtracted for the LMR (Low Mass Region) data M $< 1\,\mathrm{GeV}/c^2$ (triangles), The IMR (Intermediate Mass Region) data (closed circles) correspond to the present work.[44].

of open charm production in nucleus-nucleus collisions at SPS energies.

Recently, it was pointed out by Satz [45] that only precise measurements of both open and hidden charm production will allow the construction of observables that can provide information on the in-medium behaviour of quarkonia in a model independent way. The nuclear modification factor $R_{AA}$ (which is most commonly used to study medium effects) was measured at RHIC for high and low transverse momentum $p_T$ for both $J/\psi$ and D mesons [46, 47]. The plot in Figure 2.5 (left side) depicts high transverse momenta at which $R_{AA}$ for $J/\psi$ and D mesons are consistent. According to Satz [45], this indicats the absence of medium effects (no suppression nor enhancement) for $J/\psi$ as such effects would be seen as a deviation from the open charm $R_{AA}$. In contrast, Figure 2.5 (right side) shows that at low $p_T$ the value of $R_{AA}$(D) is consistent with unity, wheres $R_{AA}$ of $(J/\psi)$ shows significant suppression, which increases with the centrality.

Thus $J/\psi$ suppression at RHIC energies is really an effect of final state interaction. Such a study performed for different energies and centralities should reveal a new

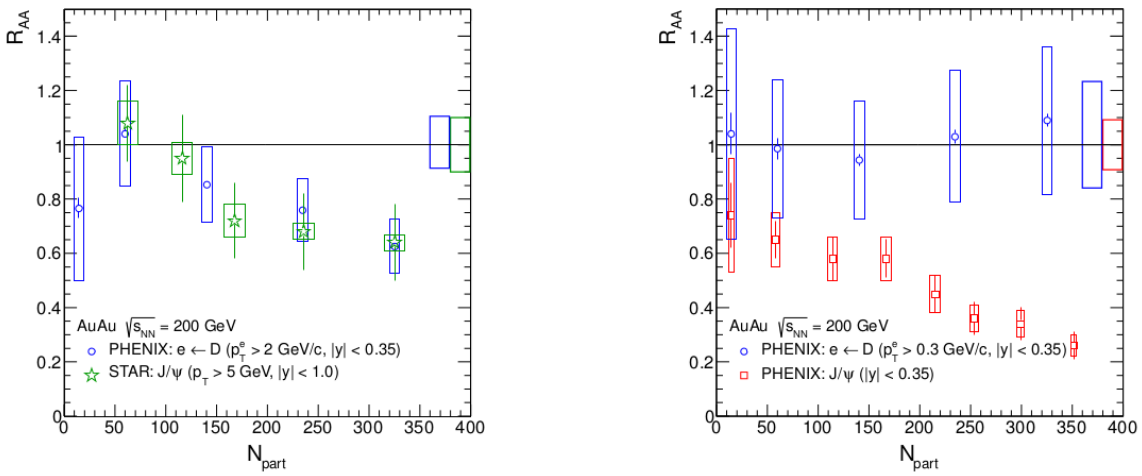


Figure 2.5: Comparison of nuclear modification factors $R_{AA}$ for $J/\psi$ production to open charm production at high (left) and low (right) transverse momenta based on RHIC data from the PHENIX and STAR experiments [46, 47, 48].

phenomenology of charm dynamics in the medium. It is important to compare hidden and open charm production in the same phase space region and to precisely measure both charm states. The measurement of D meson production from their semi leptonic decays (as done so far at LHC and RHIC) should be replaced by more accurate direct measurement. This provides the key motivation to measure open charm production in Pb+Pb collisions at the CERN-SPS.

# CHAPTER III

# NA61/SHINE experiment

## 3.1 Experiment overview

The NA61/SHINE experiment (Super proton synchrotron Heavy Ion and Neutrino Experiment) is a fixed target experiment at the CERN SPS [28]. This experiment was started in 2007 and it reuses most of the detectors of its former experiment NA49 with important upgrades. The main physics goals of this experiment include nucleus-nucleus (heavy-ion) collisions which are used to investigate the properties of the transition between quark-gluon plasma and hadron gas by energy scans with various ion beams (Be, Ar, Xe, Au, Pb) at energies from 13A GeV to 158A GeV and hadron beams (p, $\pi$) at 13 GeV/$c$ to 150 GeV/$c$ with a variety of fixed targets (C, Be, Ca, La, Au, Pb). The physics program also includes the study of high transverse momentum phenomena in proton-nucleus and proton-proton interactions. Hadron-nucleus interactions are measured to constrain the calculations of neutrino beam properties within the T2K experiment (Tokai to Kamioka, Japan) [49]. The NA61/SHINE experiment is located in the H2 beam line of the Super Proton Synchrotron (SPS) of CERN. The CERN accelerator complex is shown in the Figure 3.1 and the part relevant for the NA61/SHINE experiment is depicted in Figure 3.2.

During the normal operation with protons or ions, the beam is received from Proton Synchrotron (PS) where the energy is boosted up to 14 GeV/$c$ and delivered

to the SPS. In the SPS, protons can be further accelerated up to 400 GeV/$c$, the maximum energy attainable by the field of the bending magnets. The maximum energy per nucleon for ions depends upon the type of nucleus and scales with the charge to mass ratio Z/A. Secondary beams (ions, hadrons, electrons, muons) of energies from 10 to 360 GeV/$c$ are produced by interactions of the primary beam protons with the T2 target located at the beginning of the H2 beam line. Dipole magnets (BENDs) in the H2 beamline allows the selection of the momentum and quadrupoles (QUADs) are used to focus the beam.

## 3.2 Detector description

The NA61/SHINE detector setup includes beam position detectors (BPD), Cherenkov counters (C) and scintillation counter stations (S) located upstream of the target. The main particle tracking devices used in the experiment are two Vertex Time Projection Chambers (VTPC1 and VTPC2), a GAP TPC and two Main TPCs (MTPC1 and MTPC2). The Time of Flight detectors (ToF), which are used for hadron identification, are located behind the MTPCs. The Projectile Spectator Detector (PSD) measures the energy of projectile spectators and delivers information on the collision centrality. The experimental setup is depicted in Figure 3.3 [50]. The location of the future Vertex Detector(VD) is indicated by an arrow. It will be located downstream of the target, at a distance of about 50 cm to the front of the active VTPC1 volume. The VD detector will be able to provide precise tracking at target proximity.

### 3.2.1 Beam position detectors and trigger

The NA61/SHINE experiment uses three Beam Position Detectors (BPDs). Each BPD measures the transverse position of the trigger-selected beam particle. These

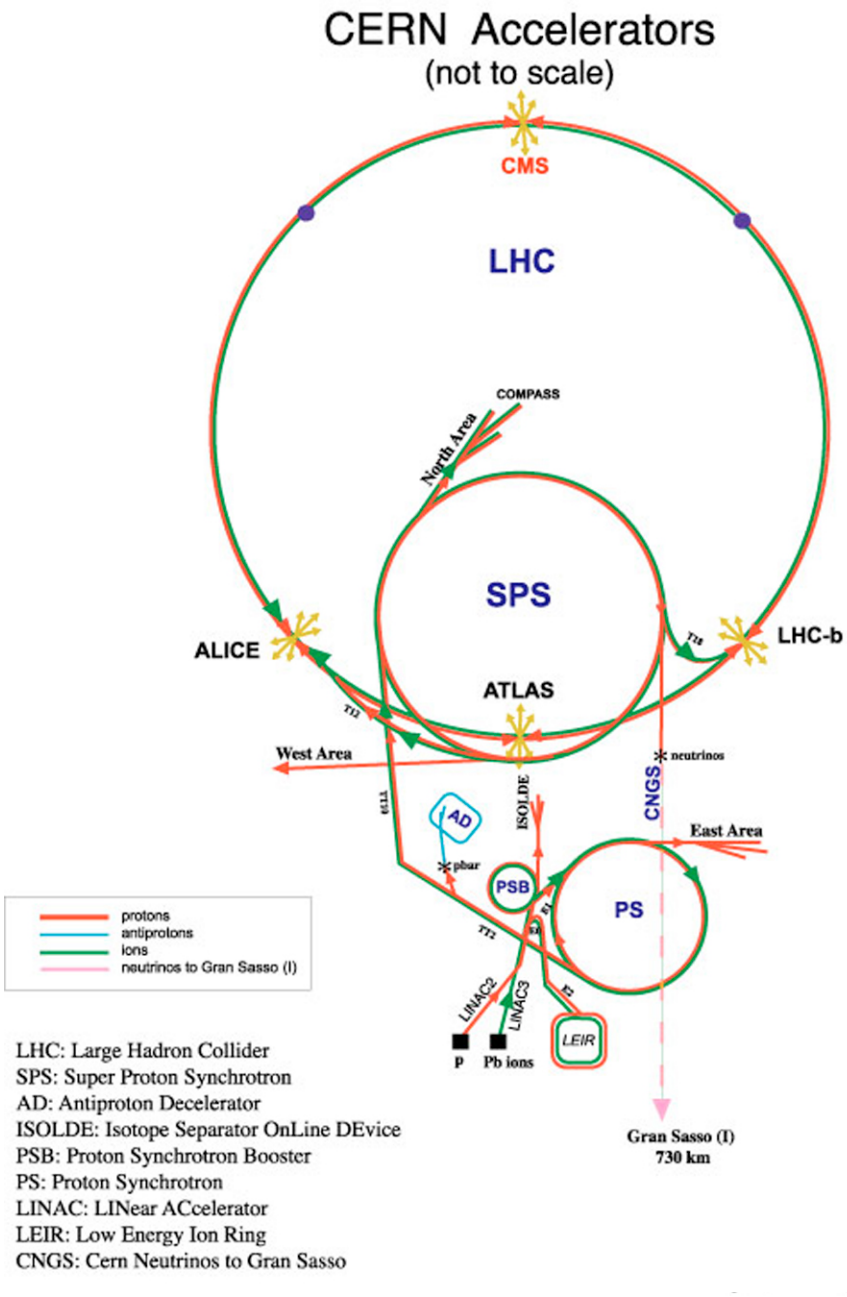


Figure 3.1: The accelerator complex of CERN [51].

detectors are basically multi-wire proportional chambers located at distances of up to 30 m upstream of the target. The chambers are filled with $Ar/CO_2$ gas mixture and are equipped with a cathode strip readout (32 strips with 1.5 mm pitch) providing a resolution of 200 $\mu$m in the orthogonal direction. The active area of the detectors is on the order of 48 $\times$ 48 mm$^2$. Each detector consists of two orthogonal wire (15

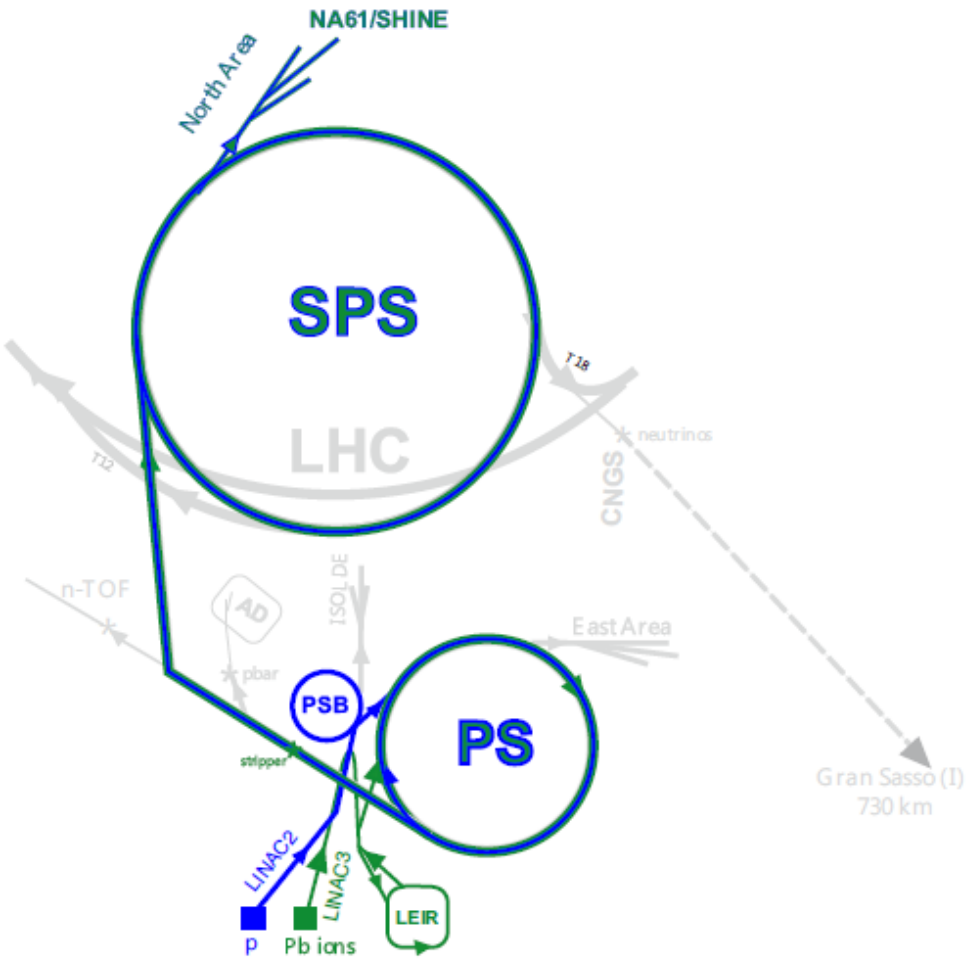


Figure 3.2: Schematic diagram of the part of the CERN accelerator complex relevant for NA61/SHINE ion and proton beam operation (top view, not to scale) [51].

$\mu$m thick tungsten) planes sandwiched between three cathode planes made of 25 $\mu$m aluminized Mylar foils. The reconstruction algorithm finds a cluster in each plane which is a set of the adjacent strips with signal amplitudes above a threshold value. In order to determine the position of the beam particle, the centroid method is used by which an average of the strip positions weighted with the signal amplitudes on the strips is calculated for the cluster.

The intersection point of the extrapolated beam trajectory with the target is used as the primary event vertex in the reconstruction. The accuracy of the beam position extrapolated to the target is 40 $\mu$m for Pb and 170 $\mu$m for proton beam [28]. The

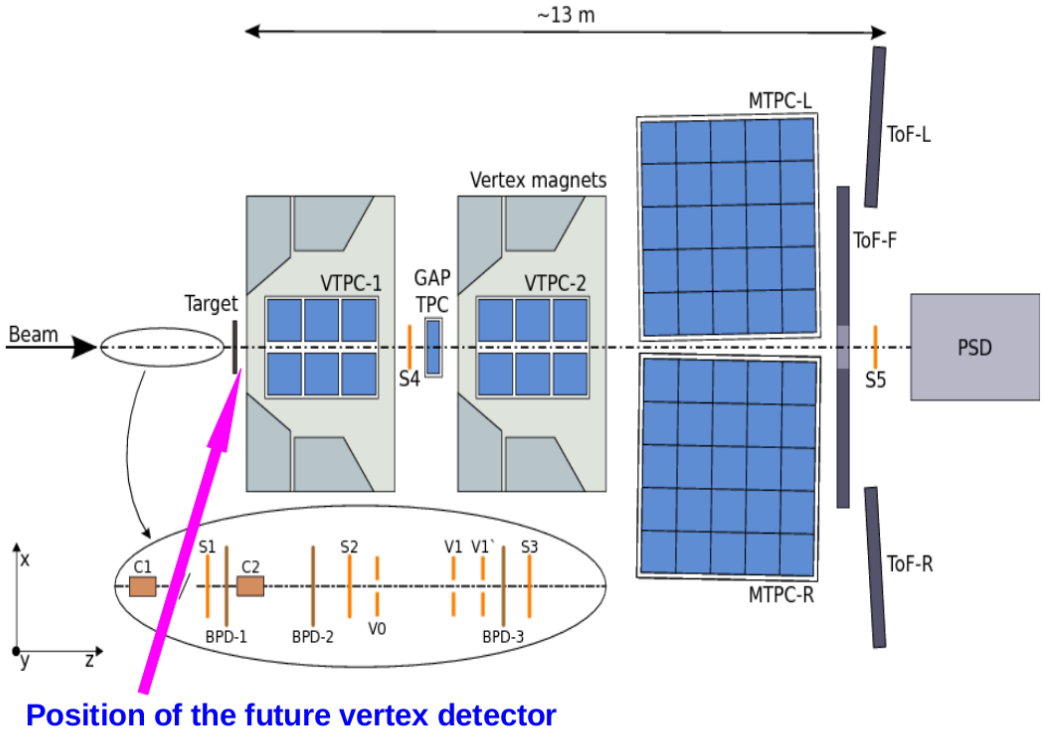


Figure 3.3: The layout of the NA61/SHINE experimental set-up (horizontal cut in the beam plane, not to scale) with indicated position of the future vertex detector.

layout of a BPD detector is shown in Figure 3.4.

The trigger system of the experiment is capable of handling and selecting different reactions for variety of beams (pions, kaons, protons, ions) and targets as required by the NA61/SHINE physics programme. The trigger decision is based on input from the scintillator beam counters, the Cherenkov detectors which identify beam particles (hadrons or ions), and the PSD calorimeter which is used for centrality selection (ion collisions).

### 3.2.2 Time Projection Chambers

Time Projection Chambers (TPCs) are used for charged particle tracking and identification in the NA61/SHINE experiment. There are four large volume TPCs,

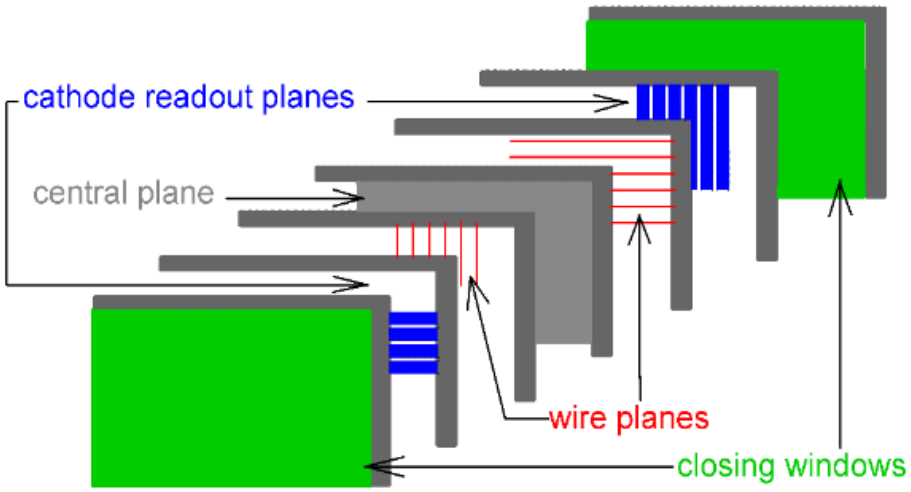


Figure 3.4: The schematic layout of a BPD detector. The cathode readout planes, the wire planes and the closing windows are shown.

two Vertex Time Projection Chambers (VTPC1 and VTPC2) and two Main TPCs (MTPC1 and MTPC2). The VTPC's are located inside the magnetic field of large aperture magnets while the MTPCs are positioned downstream of the magnets. The two identical super-conducting dipole magnets provide a maximum total bending power of 9 Tm at currents of 5000 A with field strengths of 1.5 T and 1.1 T. More details about the magnets can be found in [52].

In addition a smaller TPC (GAP-TPC) is placed between two VTPC's whose purpose is to measure particles emitted at forward angles. The TPC tracking system allows reconstruction of over 1000 tracks in a single Pb+Pb interaction. These devices consist of a large volume of gas in which particles leave a trail of ionization electrons. A uniform vertical electric field is established by a surrounding field cage which is made of aluminized Mylar strips that are kept at the appropriate electric potential by a voltage divider chain. The electrons drift with constant velocity towards the read-out chamber where their arrival time, position, and total amplitude of the signals are measured with proportional wire chambers. This process is illustrated in Figure 3.5.

The MTPCs are filled with a gas mixture of $Ar/CO_2$ in the proportion of 95/5

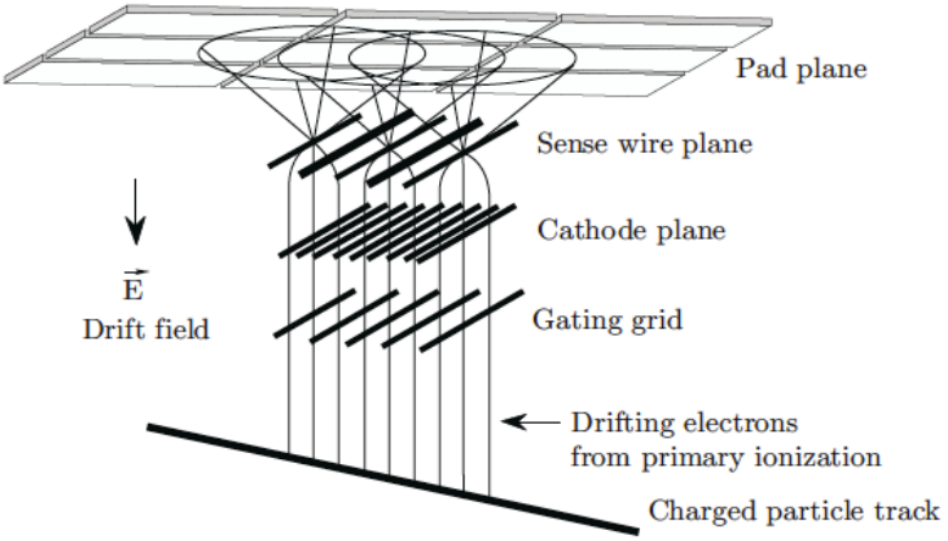


Figure 3.5: Schematic of operation of a TPC showing a charged particle traversing the sensitive volume of the detector (from [52]).

by volume and have a readout surface area at the top of 3.9 $\times$ 3.9 $m^2$ and a height of the field cage of about 1.1 m. The track signals are read out by 25 proportional chambers providing up to 90 measured points and ionization samples on each particle trajectory. The VTPC's, on the other hand employ a gas mixture of $Ar/CO_2$ in the proportion 90/10 and consist of a gas box with 2.0 $\times$ 2.5 $m^2$ top surface area and 0.67 m depth. The readout of each VTPC is performed by 6 proportional chambers on the top which provide up to 72 measurements and ionization samples on the particle trajectories. More details about the TPCs can be found in [52]. The GAP-TPC [53], located between VTPC-1 and VTPC-2, is an additional tracking device placed on the beamline. It covers the gap left for the beam between the sensitive volumes of the VTPC's and MTPC's.

In order to reduce the number of $\delta$-electrons, beam pipes filled with helium were installed in the gas volume of the VTPC's. This significantly reduces the secondary interactions which as a result suppress the background and thus also improve the uncertainty of centrality reconstruction. With He beam pipes, the number of $\delta$-electrons are reduced by a factor of about 10.

### 3.2.3 BPD-TPC alignment

The main vertex reconstruction works in such a way, that if only a BPD track is fitted, then the X,Y coordinates of the main vertex are those taken from the BPD track, irrespective of the reconstruction mode (pp/pA), where pp corresponds to the proton-proton collision system while pA is analogous to proton-nucleus collision system. This is because the BPD's transverse accuracy is better than that of the TPC's. The BPD-TPC alignment is important in order to remove the bias from the main vertex position. The determination of z position of the main vertex is different for each interaction, for pp it is fitted with the tracks from TPC, while for pA it is taken as the geometrical center of the target. The BPD-TPC alignment is applied for both pp and pA modes. For the analysis, cuts applied are as follows:

(i) T2 - standard interaction trigger used for the event selection.

(ii) Incident particle position is measured in all 3 BPD's.

(iii) Check the fit quality of the main vertex.

(iv) For the pp, the reconstructed z position of the main vertex should lie within the longitudinal dimension of the target, -590.0 cm $<$ z $<$ -570.0 cm.

(v) Only VTPC1 tracks considered to assure points close to the main vertex.

Bx, By are the impact parameters of tracks in x and y directions respectively and are defined as the difference between the back-extrapolated track transverse position at Z of the main vertex and the transverse position of the main vertex. In order to find the most probable value for the peak positions of the distributions of Bx and By, the histograms were fitted with a Q-Gaussian distribution (a special case of a Tsallis distribution given by $f(x) = \frac{\sqrt{\beta}}{C_q} e_q(-\beta x^2)$ ) [54] which gives satisfactory fit quality for most of the 2009 data sets (as apposed to Lorentzian and Gaussian distributions). This analysis is performed for several data sets from 2011 through 2013.

Four track topologies are studied separately: right side positive (RST+), right side negative (RST-), wrong side positive (WST+), and wrong side negative (WST-). Tracks which follow the standard trajectory to which the TPC pads are optimized are called right side tracks while those bend away from standard trajectory and have poor resolution are termed as wrong side tracks.

An example for Be+Be at 20A GeV from 2013 is depicted in Figure 3.6 which shows Bx, By distributions with Q-Gaussian fits and which illustrates track impact parameter for all tracks. The corrections are taken from all tracks for a single run. Figure 3.7 and Figure 3.8 shows the fit results for the topology study for Bx and By respectively, separating the four track classes which were defined above. An estimate of the systematic uncertainty is given by the average difference between the highest and lowest values of the peak positions over several runs. From a given reaction, several runs are considered to check the time stability. The corrections, i.e. the transverse shifts applied to the BPD positions, are calculated as weighted averages while errors are determined as the variance of the weighted mean.

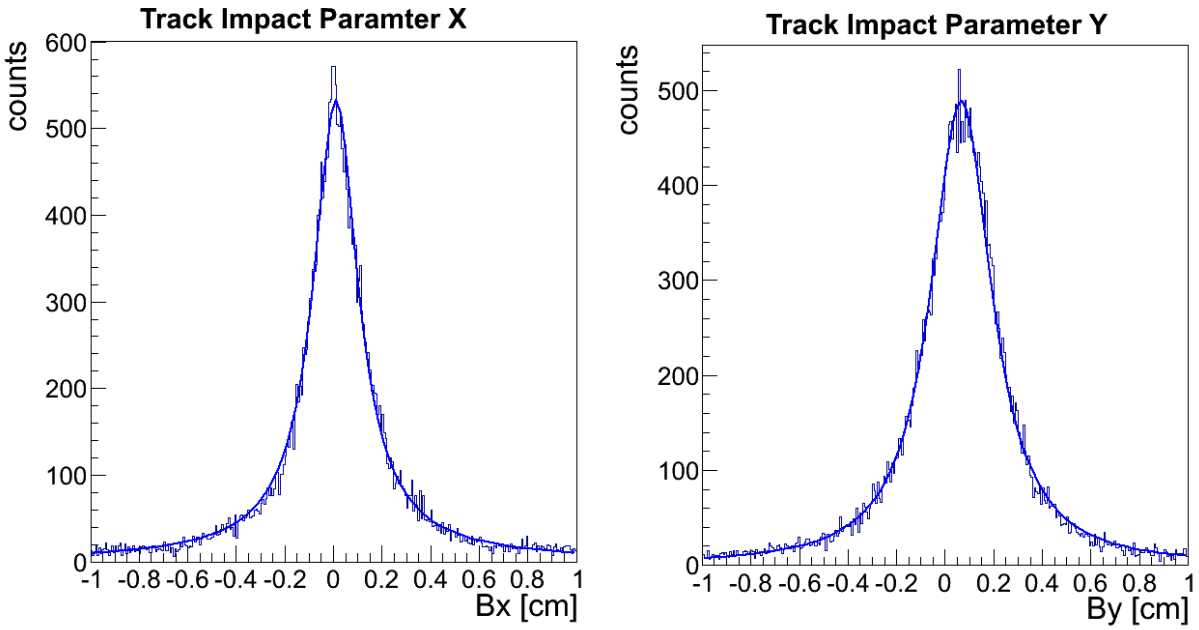


Figure 3.6: Bx,By distributions with Q-Gaussian fits

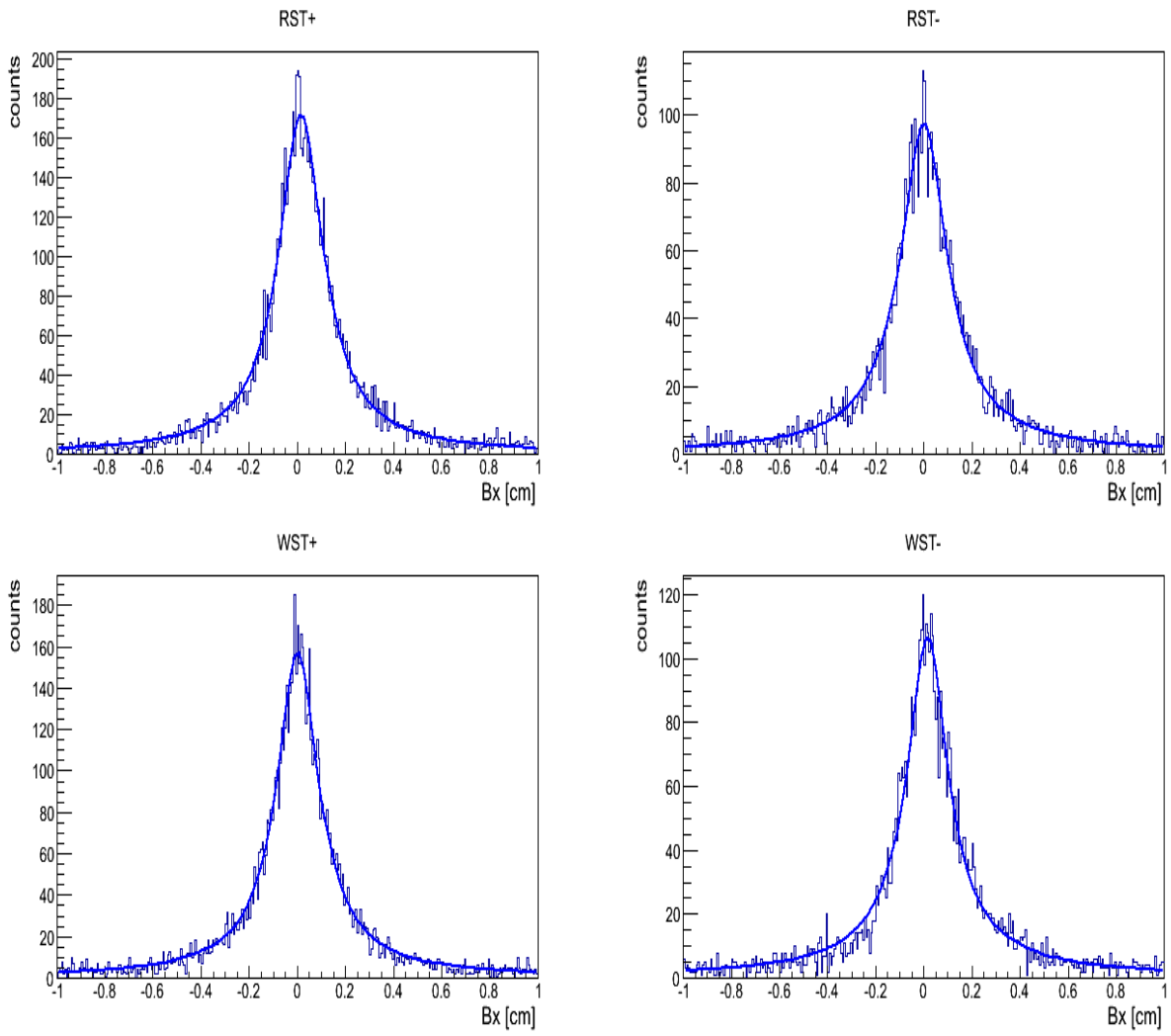


Figure 3.7: Fit results for the topology study for Bx for the Be+Be at 20 AGeV 2013 data separated into right side positive/negative and wrong side positive/negative tracks.

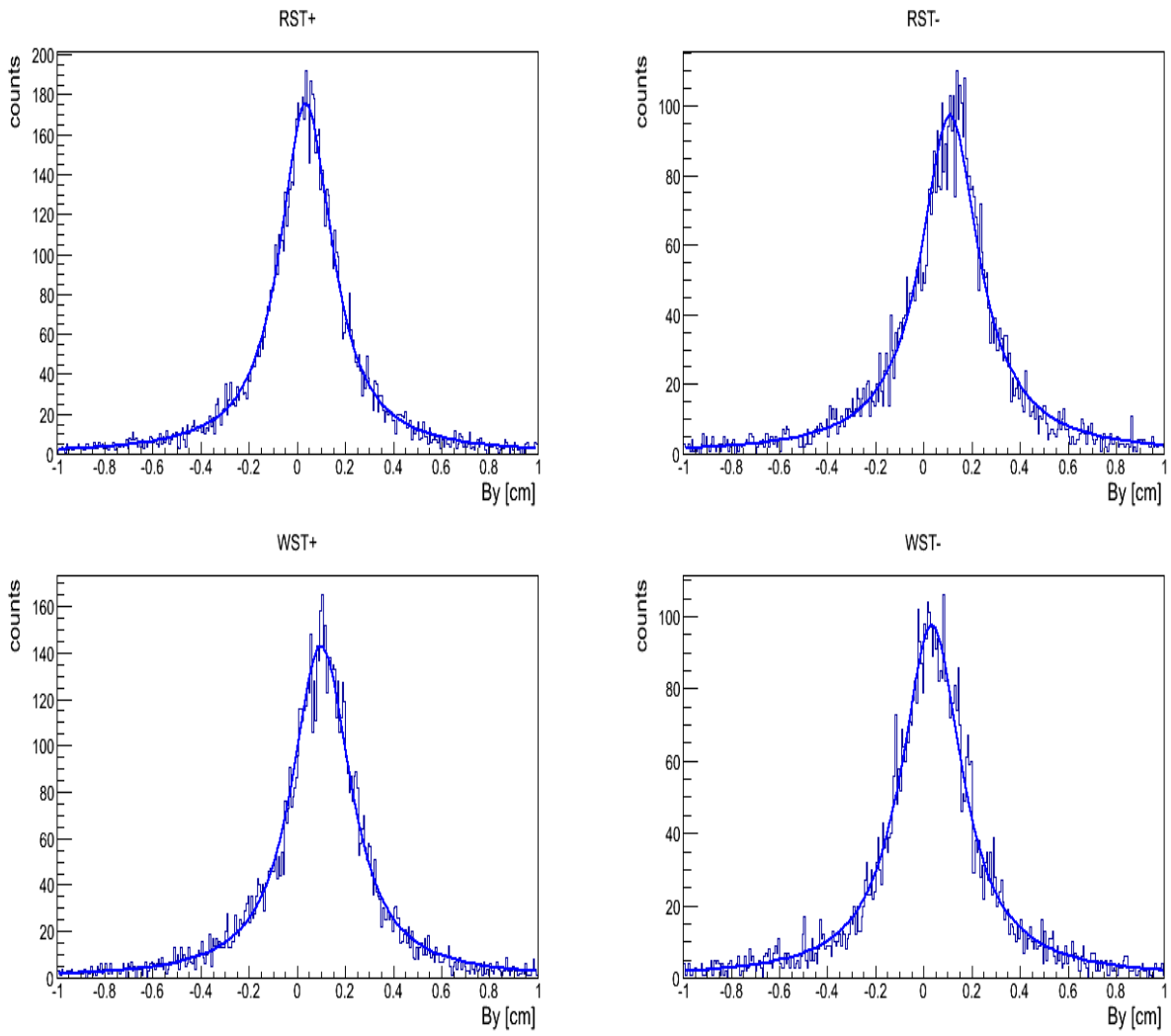


Figure 3.8: Fit results for the topology study for By for the Be+Be at 20 AGeV 2013 data separated into right side positive/negative and wrong side positive/negative tracks.

### 3.2.4 Time of Flight detector system

The Time of Flight (TOF) detectors are mainly used for hadron identification. TOF measurements supplement the particle identification by energy loss (dE/dx) measurement in the TPCs. The NA61/Shine experiment inherited two segmented time-of-flight detector walls TOF-L(eft) and TOF-R(ight) from the NA49 experiment which are depicted in the experimental setup Figure 3.3. In order to also fulfill the requirements for the T2K physics program, a new TOF-F(orward) was constructed

and is located behind the MTPCs. The particle identification (PID) method relies on combining the dE/dx measurements from the TPC's and mass-squared measurements from the ToF-F, which yields a high purity particle separation with large momentum range. At lower momenta, the ToF- F allows good particle separation while, dE/dx information is required for higher momenta. The selection of particle yields with a very high efficiency over the whole momentum range becomes feasible with the combination of both measurements. The time of flight of the particle depends upon the start signal that is given by one of the trigger detectors (S1 scintillator counter) used in the trigger logic and the stop signal produced by the readout of the TOF detector element which was hit by the particle. The TOF-F is made of 64 scintillator bars with photomultipliers (PMTs) read out at both ends. The TOF-F has a time measurement resolution of about 115 ps, while TOF-L and TOF-R have resolution of 60 ps [28]. The particles mass squared can be calculated from the time of flight t, the length l of the track trajectory, and the momentum p obtained from the TPCs.

$$m^2 = p^2(\frac{c^2t^2}{l^2} - 1) \qquad (3.1)$$

### 3.2.5 Projectile Spectator Detector

One of the upgrades of the NA61/SHINE experiment is a construction of the forward hadron calorimeter referred to as the Projectile Spectator Detector (PSD). The PSD's main purpose is to measure the energy of projectile spectators and to provide information on the centrality of nucleus-nucleus collisions. The precise event-by-event measurement of the energy of the projectile spectators allows us to determine the number of nucleons participating in the reaction. High energy resolution in the PSD can be obtained over a very broad energy range from 10 GeV to 30 TeV and it yields a low uncertainty in the determination of the number of interacting nucleons even for

peripheral collisions. The energy measurement with high precision and granularity, allows one to separate different contributions (protons, neutrons, fragments) and provides the possibility to determine the reaction plane of the event. More information on the PSD can be found in [55].

# CHAPTER IV

# Open Charm simulation

## 4.1 Simulation overview

A feasibility study was done for the measurements of $D^0$ mesons (open charm) with the NA61/SHINE experiment at the CERN-SPS via its decay into two daughter particles, a kaon and a pion. Such measurements are difficult due to the low probability of $D^0$ meson production. Various decay channels of $D^0$ mesons are listed in Table 4.1. For our simulation, we consider the two-body decay channels $D^0 \rightarrow K^- + \pi^+$ and $\overline{D}^0 \rightarrow K^+ + \pi^-$ which are easiest to measure and are considered bench mark hadronic decay channels of open charm mesons.

This study was done for central Pb+Pb collisions at the top SPS energy of 158A GeV and the lower energy of 40A GeV, as well as for Ar+Ar collisions at 158A GeV energy. For the physical input of the simulation, the AMPT (A Multi-Phase Transport Model) event generator was used to produce 200k Pb+Pb 0-10% central collision events. The AMPT model also provides a good background description which in this study include mostly charged hadrons- predominantly pions and kaons [56].

The AMPT model predicts a low average multiplicity of 0.01 for $D^0$+$\overline{D}^0$ per central Pb+Pb event. This value seems to be under predicted with respect to PYTHIA results scaled to number of binary nucleon-nucleon collisions in central Pb+Pb equal

to 0.21 [57]. The HSD (Hadron String Dynamic) model predicts a multiplicity of 0.2 (see Figure 2.2). Because the HSD model was tuned to properly describe available p+A and $\pi$+A charm production data at SPS energies [39], we scaled the AMPT multiplicities to the prediction of the HSD model. The predictions from the HSD model also seems to be consistent with the PYTHIA predictions.

Table 4.1: Hadronic decay channels [58] that are most suitable for the reconstruction of open charm mesons in the NA61/SHINE experiment.

| Meson | Decay Channel | $c\tau$ | Branching Ratio |
|---|---|---|---|
| $D^0$ | $D^0 \to K^- + \pi^+$ | 122.9$\mu$m | (3.91±0.05)% |
| $D^0$ | $D^0 \to K^- + \pi^+ + \pi^+ + \pi^-$ | 122.9$\mu$m | (8.14±0.20)% |
| $D^+$ | $D^+ \to K^- + \pi^+ + \pi^+$ | 311.8$\mu$m | (9.2±0.25)% |
| $D_s^+$ | $D_s^+ \to K^+ + K^- \pi^+$ | 149.9$\mu$m | (5.50±0.28)% |
| $D^{*+}$ | $D^{*+} \to D^0 + \pi^+$ | ..... | (61.9±2.9)% |

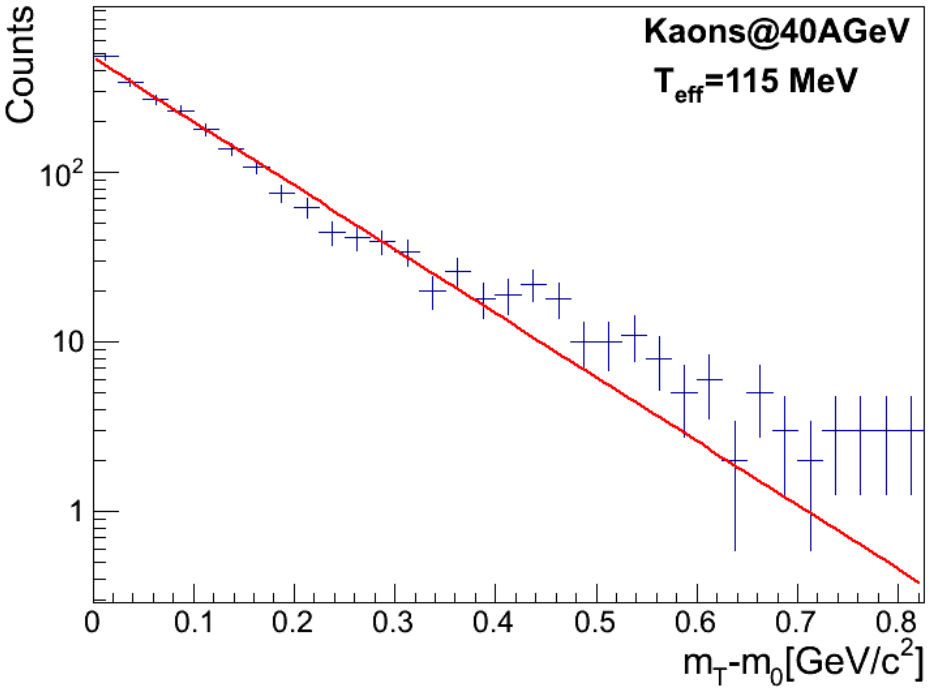


Figure 4.1: Transverse mass distribution from AMPT for kaons produced in central Pb+Pb collisions at 40A GeV. The effective temperature ($T_{eff}$) is on the order of 115 MeV.

Within the generated statistics, the AMPT event generator does not generate

significant numbers of open charm mesons at the lower energy of 40A GeV. However, we observe that the slope parameter of the transverse mass distribution and the width of the rapidity distribution for kaons do not change by more than 10% when the energy changes from 158A GeV to 40A GeV. In order to describe the phase space for $D^0$ mesons at the lower energy, we assumed changes in the shapes of $m_T - m_0$ distributions similar to those observed for kaons. Figures 4.1 and 4.2 depict the transverse mass distributions for kaons at 40A GeV and 158A GeV with effective temperature ($T_{eff}$) is on the level of 115 MeV and 120 MeV respectively.

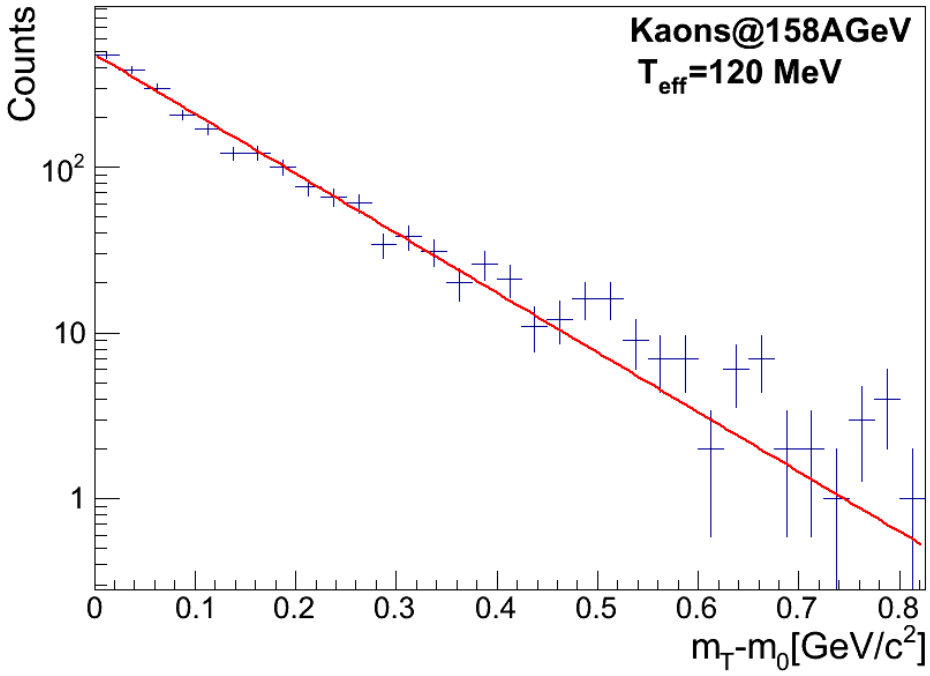


Figure 4.2: Transverse mass distribution from AMPT for kaons produced in central Pb+Pb collisions at 158A GeV. The effective temperature ($T_{eff}$) is on the order of 120 MeV.

Figure 4.3 shows the illustration (from GEANT4) of the $D^0$ meson decay into its daughter particles $K^-$ and $\pi^+$. This figure shows the helium vessel including the target and four Vertex Detector (VD) stations. The red and blue tracks represent the daughter particles $K^-$ and $\pi^+$ respectively. The $c\tau$ (the decay path length)

of $D^0$ mesons is approximately $123\,\mu$m. In order to distinguish between primary and secondary vertices, a high resolution detector is required. Thus our feasibility study also addresses the issue of VD optimization with emphasis on the prospect of developing a VD based on CMOS technology.

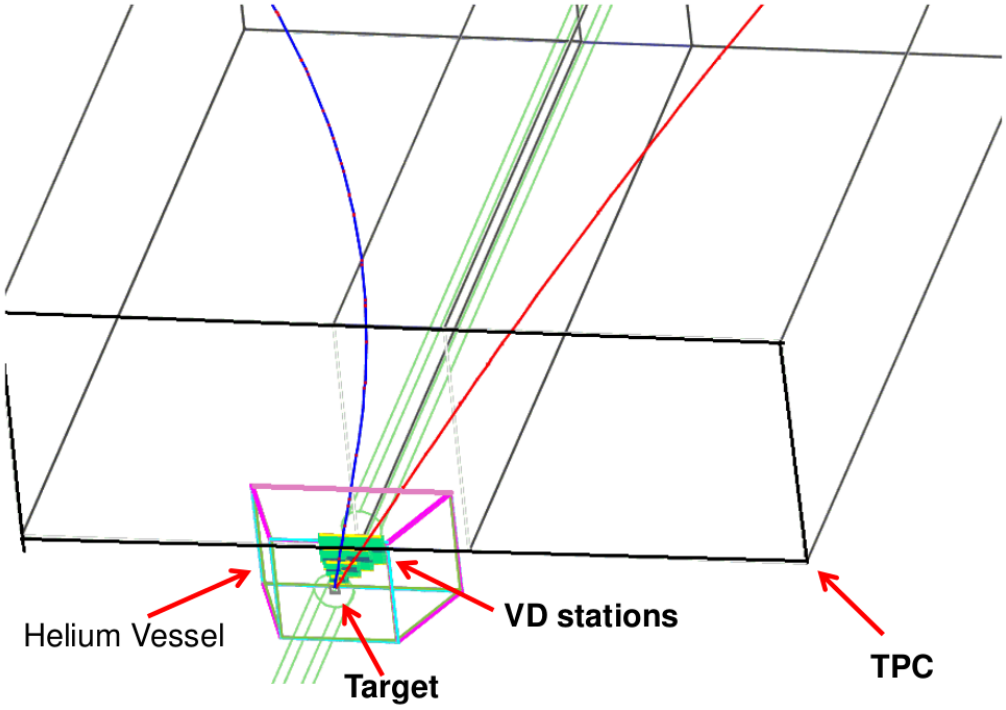


Figure 4.3: Decay of a $D^0$ meson into two daughter particles kaon (blue track) and pion (red track) as seen by the VD and VTPC1. Also the helium vessel, the target, the VD stations and the Time Projection Chamber (TPC) are shown in outline.

### 4.1.1 The AMPT model

In order to understand the numerous observables measured at the RHIC (Relativistic Heavy Ion Collider) e.g. rapidity distributions and elliptic flow, transverse momenta and centrality dependences of various particles, many theoretical models have been developed. These models include the thermal models [59, 60] based on the assumption of global chemical and thermal equilibrium, the hydrodynamic models [61, 62] based only on the assumption of local thermal equilibrium, and transport

models [63, 64] that treat non-equilibrium dynamics explicitly.

The AMPT was developed to describe non-equilibrium many-body dynamics. This model simulates nuclear collisions for both p+A and A+A systems for energies in the range of about $\sqrt{s_{NN}} = 5$ (AGS) to 5500 GeV (LHC). It includes initial parton interactions, the transition between parton and hadron phases of matter, and hadron interactions [65, 66]

The AMPT model consist of four main components:

1. simulation of initial conditions which are given by the HIJING model [67, 68] and include the momentum and spatial distributions of minijet partons,

2. modelling of parton interactions by Zhang's Parton Cascade (ZPC) model [69],

3. conversion between parton and hadron matter by the Lund String Fragmentation model [70, 71] in which strings are stretched between the interacting partons and the resulting strings are converted into hadrons

4. and finally the scatterings among the resulting hadrons are described by a relativistic transport (ART) model [72].

ART is the relativistic transport model developed for Alternating Gradient Synchrotron energies. Figure 4.4 shows the rapidity distributions of negatively charged particles (upper left), of net-protons (upper right), charged kaons (lower right) and charged pions (lower left) in central Pb+Pb collisions at the CERN-SPS. Experimental data for the 5% most central Pb+Pb collisions from the NA49 Collaboration [73, 74] are compared to calculations using the AMPT model (curves). It is seen that the AMPT model is able to make predictions with an accuracy of $\approx 20\%$ for charged particles multiplicities.

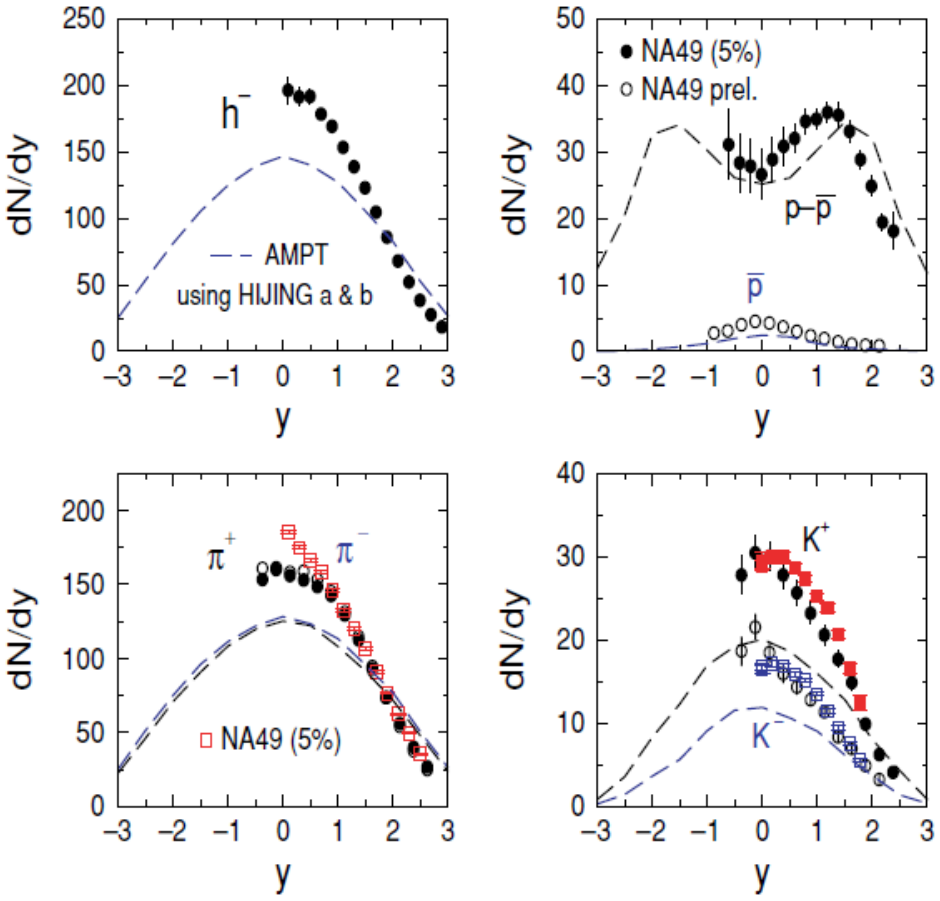


Figure 4.4: Rapidity distributions in central (b = 3 fm) Pb+Pb collisions at $\sqrt{s_{NN}}$ = 17.3 GeV. Circles and squares are experimental data, while dashed curves are results from the AMPT model using default a and b parameters as in the HIJING model [56].

### 4.1.2 Vertex Detector model

In our simulation GEANT4 is used to describe the particle transport through the NA61/SHINE experimental setup supplemented with the future VD. The VD modelled in GEANT4 consists of four VD Stations (VDS1, VDS2, VDS3 and VDS4) located at distances of 5 cm, 10 cm, 15 cm, and 20 cm downstream of the target respectively. The external transverse dimensions of the stations are $2 \times 4\,\mathrm{cm}^2$ (VDS1), $4 \times 8\,\mathrm{cm}^2$ (VDS2), $6 \times 12\,\mathrm{cm}^2$ (VDS3) and $8 \times 16\,\mathrm{cm}^2$ (VDS4). More than 99% of pions and kaons originating from the decay of $D^0$ mesons are detected by stations of

these dimensions.

Each station consists of a layer of silicon with thickness of 50$\mu$m, an epoxy glue layer of 50$\mu$m and a carbon fiber carrier of 300$\mu$m. In order to let the beam ions pass without interaction, the central part of each station has a square hole of size $3\times3\,\mathrm{mm}^2$. The stations and the target are enclosed in an aluminium vessel as depicted in Figure 4.5. The vessel is equipped with thin front and back kapton windows and is filled with helium gas at atmospheric pressure to minimize multiple scattering of the produced particles.

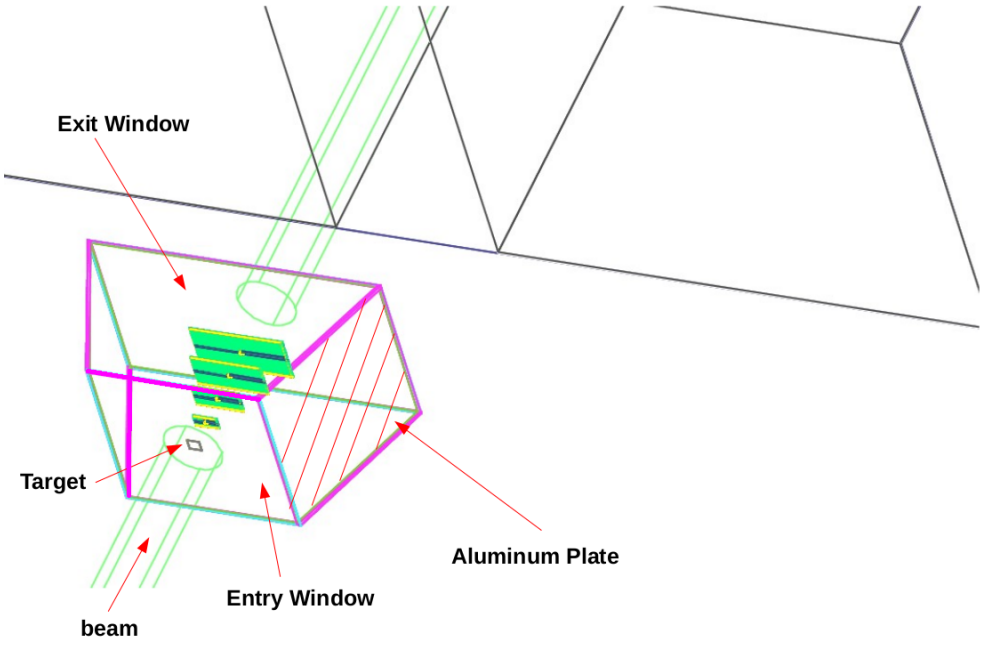


Figure 4.5: The helium vessel containing four VD stations, the carbon fiber supports and water cooling tubes.

## 4.2 Vertex Detector environment and performance

During the sensor exposure time (115.2 $\mu$s) the devices will collect particles produced in hadronic nucleus-nucleus interaction as well as $\delta-$electrons produced by beam ions passing through the target. In order to obtain more quantitative pre-

dictions on the radiation load and requirements for the two-particle separation we generated a sample of minimum bias Pb+Pb collisions at 158A GeV for the first type of particles. To account for the $\delta-$electrons, we simulated electromagnetic interactions of Pb beam ions passing through the 200 $\mu$m thick Pb target. The anticipated beam intensity in the spill during data taking is $10^5$ Hz which leads to 500 Hz hadronic interactions in the target.

### 4.2.1 Vertex detector occupancy

From the numbers above one can estimate the probability of recording only a single hadronic interaction in one frame to be about 5 %. At the same time the sensor will collect on average $\approx 10$ bunches of $\delta-$electrons generated by passing beam ions.

The most critical area is the first Vertex Detector station (VDS1) where the track occupancies are about 5 tracks/mm$^2$/event for 0-10% central Pb+Pb collisions shown in Figure 4.6 (right) and 1.6 tracks/mm$^2$/event averaging over minimum bias Pb+Pb collision shown in Figure 4.6 (left), and 0.04 $\delta-$electrons/mm$^2$/event from the Pb ions traversing the 200 $\mu$m Pb target is depicted in Figure 4.7. The occupancy significantly decreased towards the outer regions of VDS1.

The probability of an empty frame is 95%, of a single event is 4.7%, and for pile-up is 0.12%. In case of one pile-up (one center and one semi-peripheral event) the probability of single pixel occupancy is on the level of 0.25% including 0.01% contribution from $\delta-$electrons. Even in the very challenging case when one central and one semi-peripheral Pb+Pb event is collected in one frame, the estimated single hit occupancy in the most illuminated part of the sensor is 0.75 %. To get the last value we assumed that one particle hitting the sensor generates a cluster containing on average 3 pixels [75].

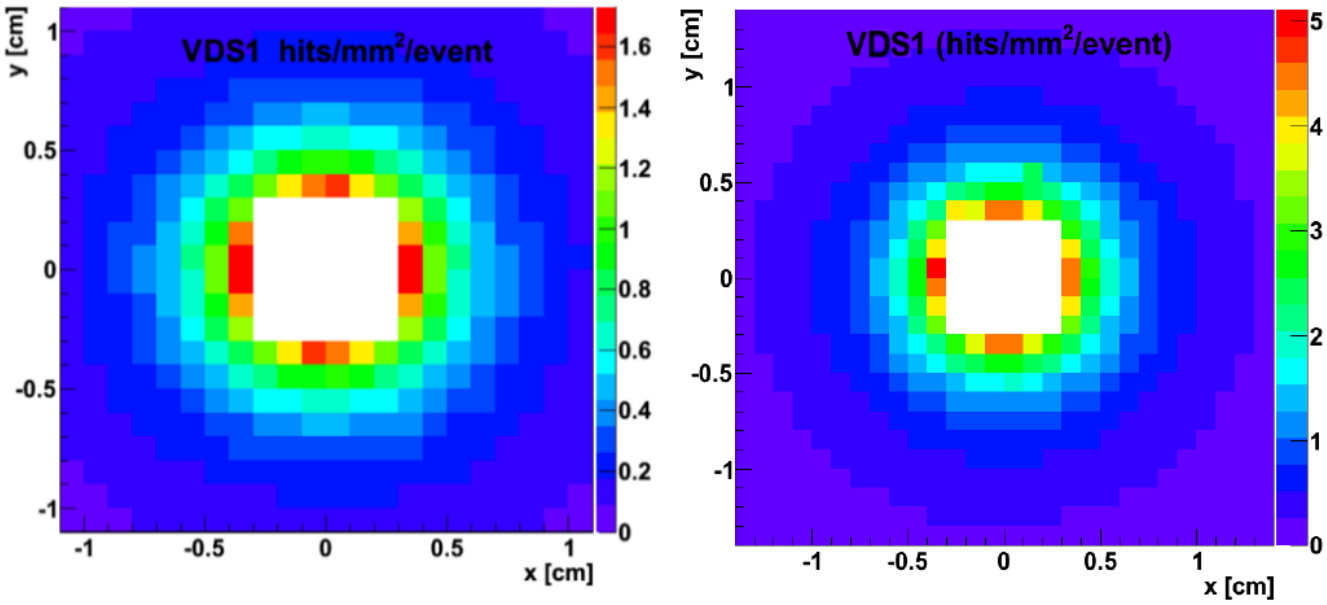


Figure 4.6: Hit occupancy for the most inner part of the detector. Left: the hit occupancy for minimum bias Pb+Pb collision, Right: the hit occupancy for the 0-10% central Pb+Pb collisions. The scale refers to the average number of hits/mm$^2$/event.

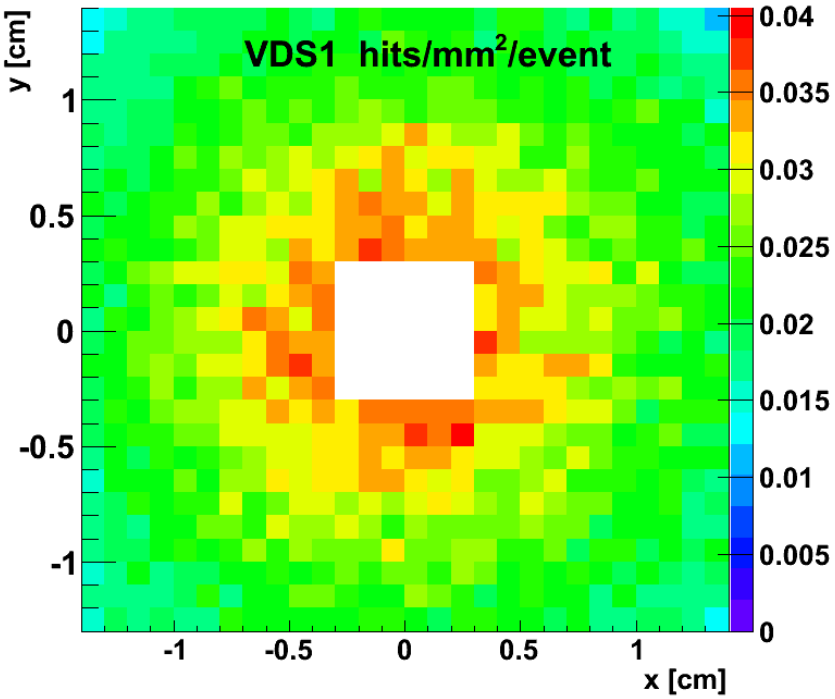


Figure 4.7: The hit occupancy for $\delta-$electrons/mm$^2$/event from the Pb ions traversing the 200 $\mu$m Pb target.

### 4.2.2 Size of VD stations

The hit distribution (x,y) generated by signal tracks in the first vertex detector station (VDS1) is depicted in Figure 4.8. It is observed that for VDS1 99.5% of signal tracks are localized within the $2\times$ 4 cm$^2$ box indicated by the dotted black lines. Note that in order to cover the remaining 0.5% one needs to extend the station in the X direction almost by a factor of 2. For the stations VDS2, VDS3 and VDS4 stations we just extended the size of these stations in proportion to their distance from the target and obtained 0.7%, 0.8% and 0.9% of signal tracks lost outside the defined station dimensions respectively.

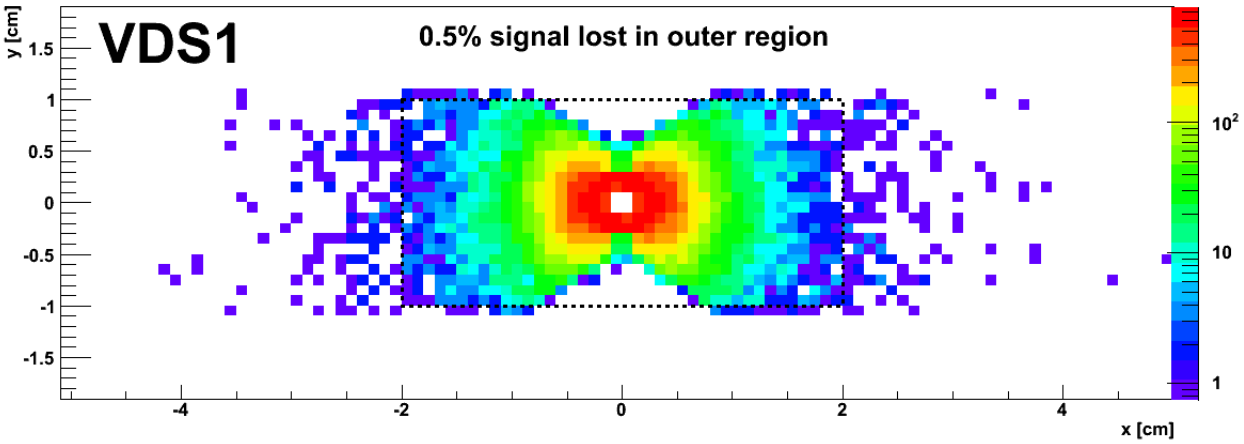


Figure 4.8: Distribution of hits in the first vertex detector station (VDS1).

### 4.2.3 Fluence estimates

It is expected that during the data taking period the VD will be exposed to a high level of radiation. The sensor performance can deteriorate due to the effects of non-ionizing energy loss (NIEL) see Figure A.1. In order to perform the fluence estimates, two sources of particles are considered, namely, particles produced in hadronic nucleus-nucleus interactions and $\delta-$electrons. In case of this application the particles that mainly contribute to hadronic interactions are pions and protons. Based on

the anticipated beam intensity and the interaction rates the particle fluxes through the VD detector have been calculated. Integrating the fluxes over 1 month (in 1-2 months NA61/SHINE can collect about 50M central Pb+Pb events) and by using the so-called displacement damage function [90] (see appendix), we obtained the values on the level of $2.6 \times 10^{10}\,\mathrm{n}_{eq}/\mathrm{cm}^2$ and $4.2 \times 10^{10}\,\mathrm{n}_{eq}/\mathrm{cm}^2$ for $\delta-$electrons and hadrons, respectively in the most illuminated area of the sensors. Tests of MIMOSA-26 (Minimum Ionizing MOS Active pixel sensor) sensors in proton beam proved that these devices can handle fluences up to $3\times10^{12}\,\mathrm{n}_{eq}/\mathrm{cm}^2$. So this radiation tolerance provides a large safety margin for use in NA61/SHINE application [76].

## 4.3 Track reconstruction

Track reconstruction is based on the hits generated by a particle traversing the VD (VDS1-VDS4) stations and Vertex Time Projection Chambers (VTPC1 and VTPC2). The tracks which are accepted in the VTPC detectors are only considered. Similarly to the standard NA61/SHINE data reconstruction procedure, the track length in the active volume of the two VTPC's must be greater than 80 cm. The magnitude of the reconstructed track momenta is smeared out according to the experimental momentum resolution of NA49 [52].

The position resolution for each station is assumed to be $4\,\mu$m which is consistent with the results obtained during beam tests of a telescope based on MIMOSA-26 sensors [76]. The realistic tracking is based on Hough Transform (HT) which is basically a feature extraction technique and is discussed in the following section.

### 4.3.1 Hough Transform

The HT method was introduced and patented by Paul Hough in 1962 [77]. The main purpose for the HT was to detect straight lines in the pictures. The original transformation equation based on the slope-intercept parametrization of lines, was

improved by Richard Duda and Peter Hart, in 1972 to identify positions of arbitrary shapes, most commonly circles or ellipses, and it was named the generalized Hough Transform [78]. The main application of this technique in particle physics was to identify lines and arcs in the photographs obtained from cloud chambers. The technique was improved by the use of angle-radius parametrization given by the following equation.

$$r = x\cos\theta + y\sin\theta \qquad (4.1)$$

The HT procedure is based on the normal parametrization of a line in two dimensions. A straight line can be specified with such parametrization by its distance r from the origin and the angle $\theta$ of its normal, see Figure 4.9. The line detection procedure is normally implemented by considering the quadruled grid as a two-dimensional histogram or array of accumulators. The HT has many interesting features which can be utilized in many applications e.g. simultaneous detection of several lines and it is also very robust to noise produced by isolated noisy measurements.

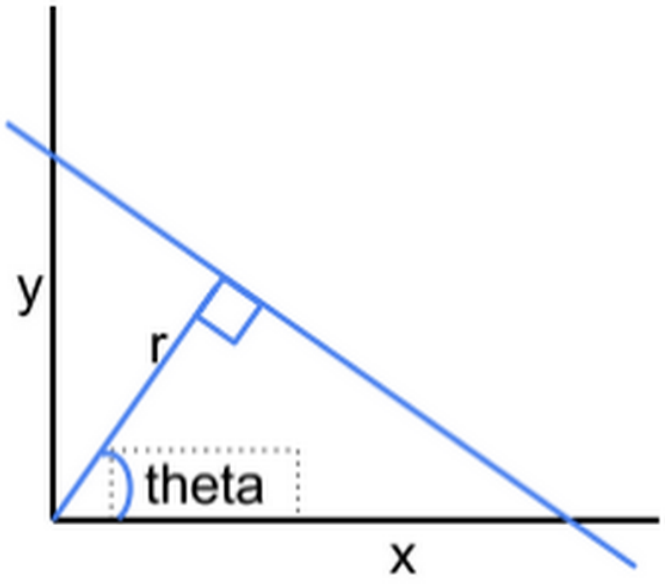


Figure 4.9: Concept of hough transform, normal straight line parametrization.

### 4.3.2 Tracking Algorithm

The realistic tracking algorithm in our simulation is based on the HT technique using slope parameters. For each VD station we performed a simultaneous transformation in the $x$ and $y$ direction assuming a narrow corridor for the track origin. Thus, for each hit we obtain $a_x$ and $a_y$ slope parameters plotted in a 2D histogram as shown in Figure 4.10. This procedure examine every station, so if e.g. there are 4 hits generated by single track, they should be described by same $a_x$ and $a_y$ parameters generating 4 counts in one bin or due to some hit position spread, these 4 counts are spread into the neighbouring bins. The Figure 4.10 shows the HT space for 1 event in Ar+Ar reaction at 158A GeV energy. One can see from figure, that the bins with three or more counts which are generated by tracks are located in the central region. The bins with one count only are due to the fake hits included in the reconstruction procedure. We assumed a fake rate on the level of $10^{-4}$/pixel/frame which was determined by the test measurement of MIMOSA-26 sensors [76]. These fakes are a feature of MIMOSA-26 sensors and are due to statistical charge fluctuations (thermal noise) in silicon.

In order to handle the cases where hits generated by one track split into the neighbouring (2,3 or 4) bins the clusterization procedure was developed. Two such cases are shown in Figure 4.11. The big squares refer to the number of counts in a specific bin. These counts if not 0, are shown by drawn numbers. The small squares show the location of GEANT track in $a_x$ and $a_y$ space. Note, that the bin size used in the 2D histogram is 1.5 times bigger than the average experimental cluster size in $a_x$ and $a_y$ space generated by one track.

The clusters which contain at least 3 hits on at least three different stations are considered for the analysis. The tracks are extracted from clusters by fitting each possible combination of hits occupying different stations with a weighted linear regression. A track is created for a $\chi^2$ value less than the predefined cut value. The

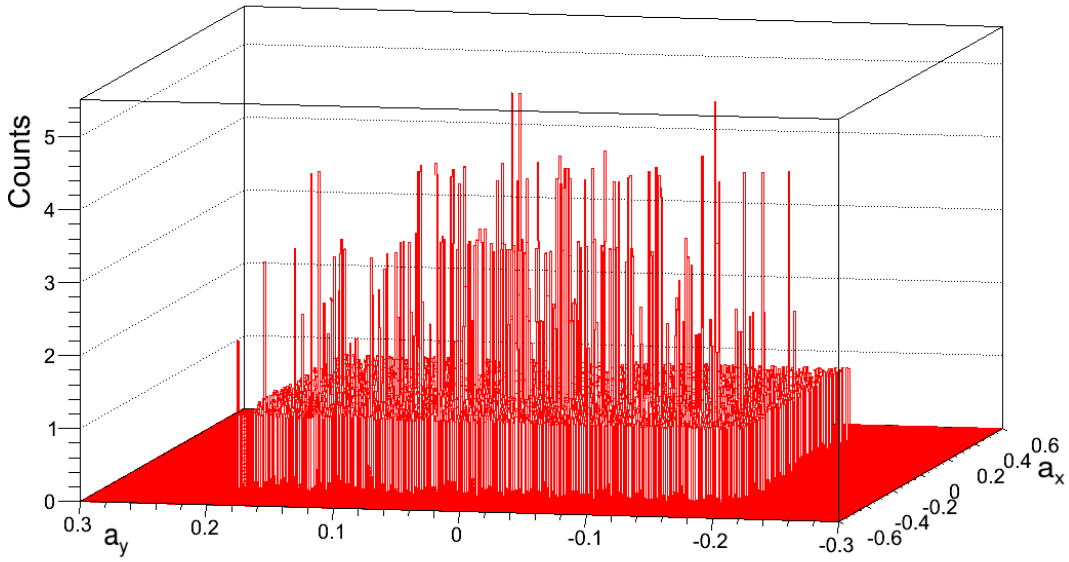


Figure 4.10: The reconstructed tracks are represented for 1 Ar+Ar reaction event in HT space at 158A GeV energy.

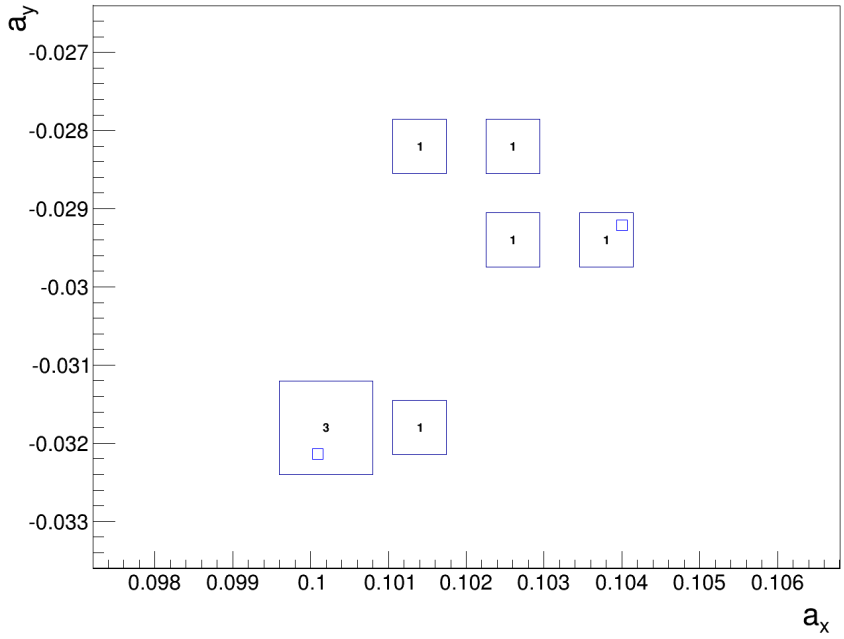


Figure 4.11: The clusterization procedure, the big squares refer to the number of counts in a specific bin. These counts if not 0, are shown by drawn numbers. The small squares show the location of GEANT track in $a_x$ and $a_y$ space.

track extraction procedure allows one to extract tracks from the two merged "track-clusters "with the number of hits on the level of 8.

The track set generated from one cluster is cleaned in such a way that, among two or more tracks sharing same first hit, the track with the smallest $\chi^2$ is selected. Figure 4.12 shows the tracking results for 1 event in the selected region of $a_x$ and $a_y$ parameters in HT space. In the figure the reconstructed tracks are represented by circles (red color), while squares (blue color) depict the initial GEANT tracks. The numbers represent the counts in HT space. One can see that in the selected region almost every GEANT track is reconstructed which indicate, that the described tracking algorithm is very efficient. More quantitative studies of tracking efficiency and fake-track contamination will be provided in section 4.3.4.

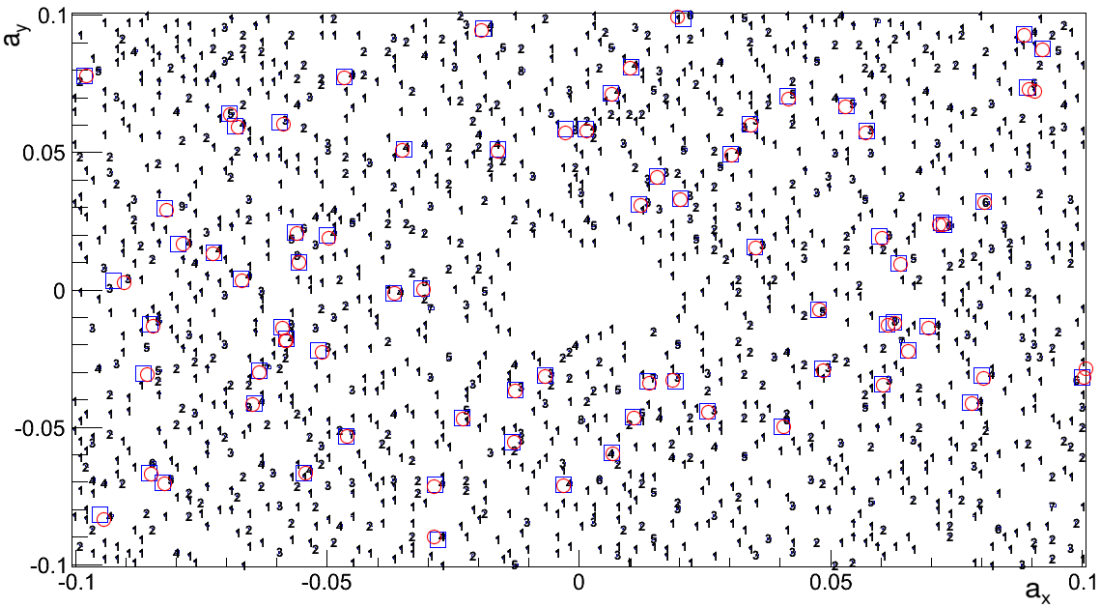


Figure 4.12: The tracking results for 1 event, in the selected region of $a_x$ and $a_y$ parameters in HT space. In the Figure squares represent GEANT tracks (blue color), while circles depict reconstructed tracks (red color), the numbers represents counts in HT space.

### 4.3.3 Track matching

Within a stand alone VD detector tracking concept, the VD tracks contain only topological information and have to be matched with VTPC tracks to obtain information about track momentum and PID (Particle Identification). The matching is done on the plane defined by entry windows of VTPC1. The tracks reconstructed in VD (VdTracks) are extrapolated in the forward direction to the matching plane. For VTPC tracks two cases are considered. If a track hits the entry window of VTPC1 the extrapolation is not required. If however, the track enters the active volume of VTPC1 for $z > z_{match}$ or enters only VTPC2, it is extrapolated backward in a uniform magnetic field to the matching plane. This matching procedure in illustrated in Figure 4.13 where the extrapolated VD and VTPC tracks are represented by red and yellow arrows respectively with tails at the matching plane.

To verify whether the extrapolated VD and VTPC tracks match to each other (belong to the same particle) we define positions and slope differences at a matching plane in the horizontal ($dx$, $da_x$) and vertical ( $dy$, $da_y$) directions. The distributions of $dx$, $dy$, $da_x$ and $da_y$ for all possible combinations of VD and VTPC tracks are shown in Figure 4.14.

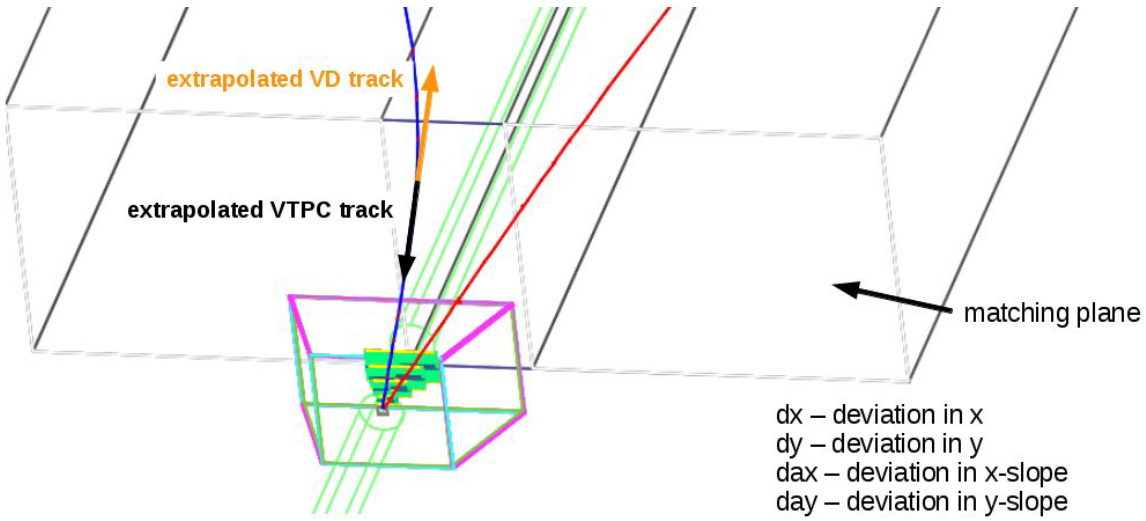


Figure 4.13: Illustration of VD and VTPC track matching.

The peaks located at 0 on top of the large combinatorial background are related to the right matching and are clearly seen for each parameter. Applying a simultaneous cut on each parameter significantly reduces the background and allows for right tracks selection.

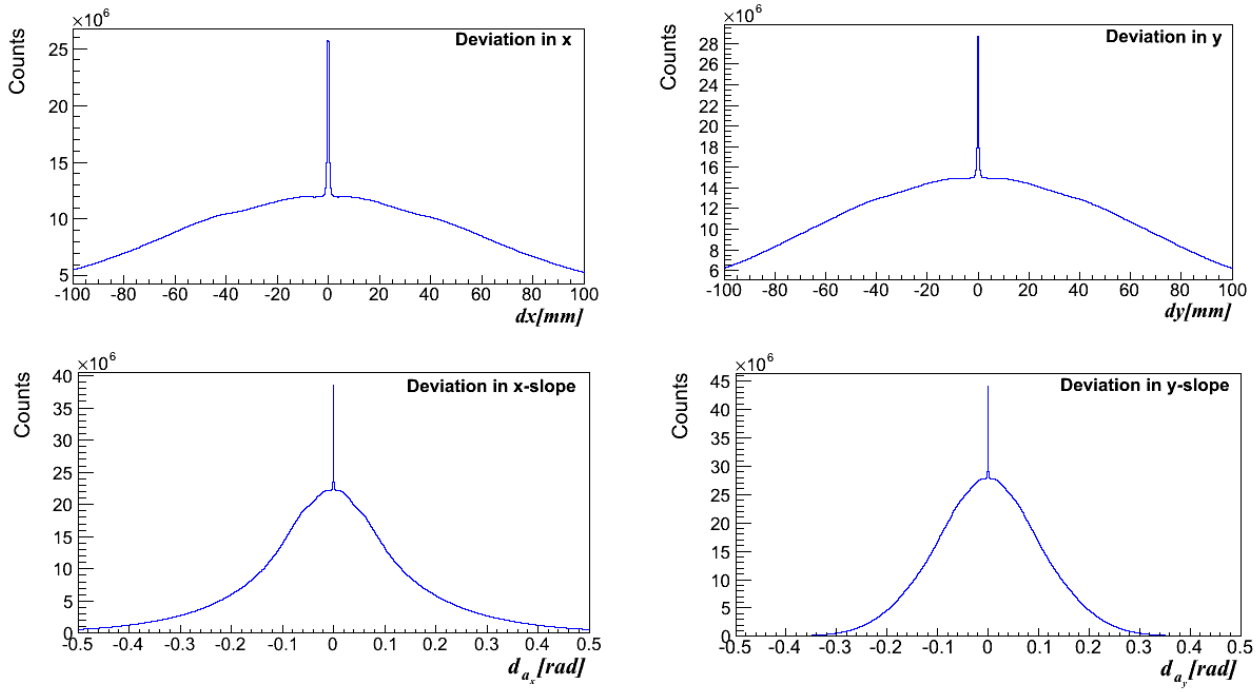


Figure 4.14: The distributions of $dx$, $dy$, $d_{a_x}$ and $d_{a_y}$ for all possible VD and VTPC tracks.

Moreover it was found, that the widths of the matching peaks noticeably depend on a track's momenta which accounts for the use of momentum dependent cuts. In Figure 4.15 I plotted the distribution of $dx$ versus track momentum. It is clearly seen that the $dx$ is much broader at lower momenta due to multiple scattering effects. The solid lines on the plot show the polynomial fit to a $1\sigma$ deviation in $dx$. As it was difficult to obtain a single fit in the whole range, two different fits were performed, one for $0 < p_T < 5$ GeV/$c$ (red line) and another for $p_T > 5$ GeV/$c$ (blue line). Figure 4.16 shows the distribution of a variable, $\Delta$, which represents the deviation from a perfect matching (in space of $dx$, $dy$, $da_x$ and $da_y$) in the units of $\sigma$, and which is

defined by the equation 4.2

$$\Delta = \sqrt{\frac{dx^2}{\sigma_x^2} + \frac{dy^2}{\sigma_y^2} + \frac{d_{a_x}^2}{\sigma_{a_x}^2} + \frac{d_{a_y}^2}{\sigma_{a_y}^2}}. \qquad (4.2)$$

The $\sigma$ values for each of the four parameters depend upon the momentum, and are calculated from the fit as illustrated in Figure 4.15. The red line shows $\Delta$ for all possible VD and VTPC track pairs, while the blue line shows $\Delta$ only for the true combination. It is seen that cut on the level of $\Delta_{cut} = 5$ allows one to select 99.5% of true combinations with the random matching contamination on the level of 0.3%.

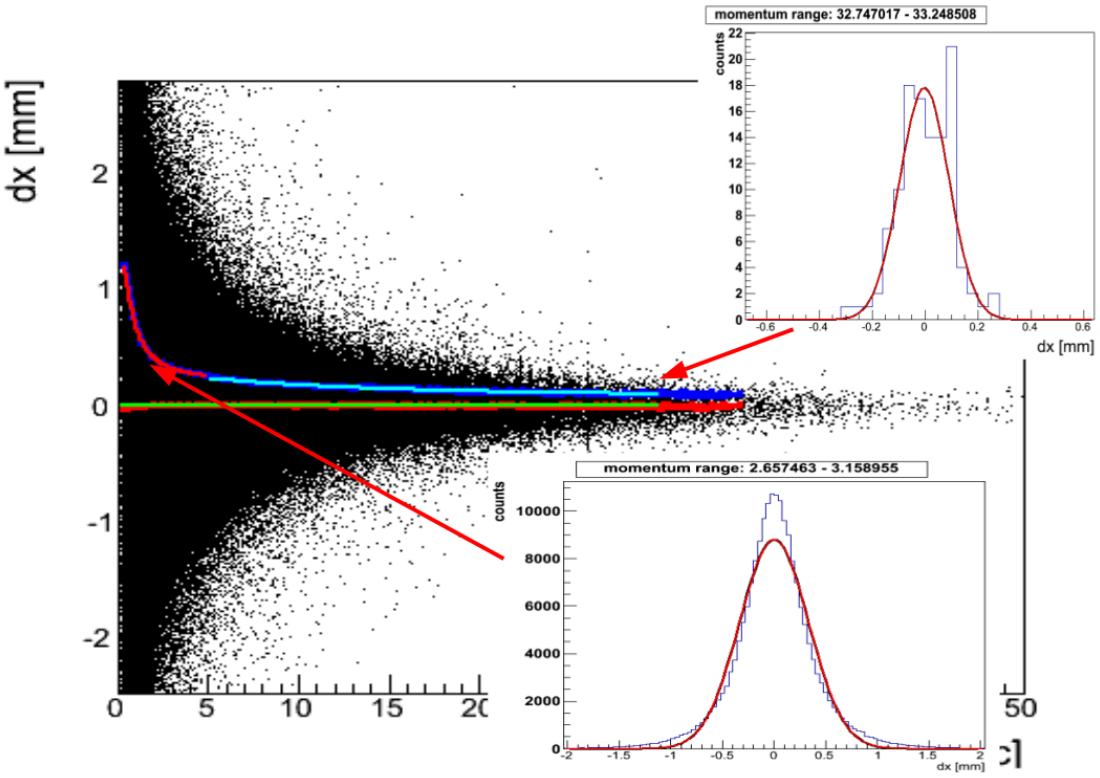


Figure 4.15: Distribution of $dx$ versus track momentum. Inserts show $dx$ distribution at the two selected ranges of the momentum.

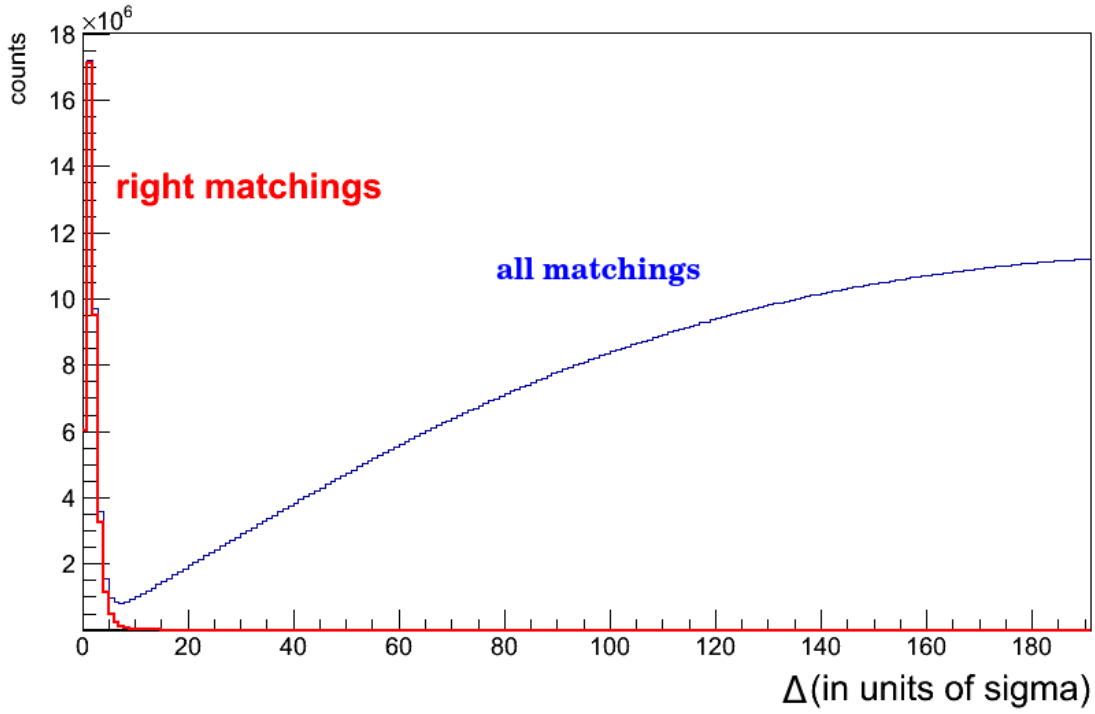


Figure 4.16: Distribution of $\Delta$ variable (for definition see text) where red line shows right matchings while blue line illustrates all matchings.

### 4.3.4 Performance of tracking procedure

To diagnose performance of the tracking procedure we developed a methods for calculating the tracking efficiency and fake contamination. The track efficiency is the ratio of reconstructed tracks that match any of the GEANT reference track to the number of all GEANT reference tracks. We select primary tracks and tracks that originate from the $D^0$ while the tracks originating from hyperon decays are not well tracked by the current algorithm, and thus are excluded. In the analysis the fake tracks are those tracks which has no correspondent GEANT track. Thus the fake contamination is defined as the ratio of number of all reconstructed tracks minus the number of reconstructed tracks that match any of the GEANT reference track to the number of all reconstructed tracks.

Figure 4.17 and Figure 4.18 represent the tracking efficiency and fake contamina-

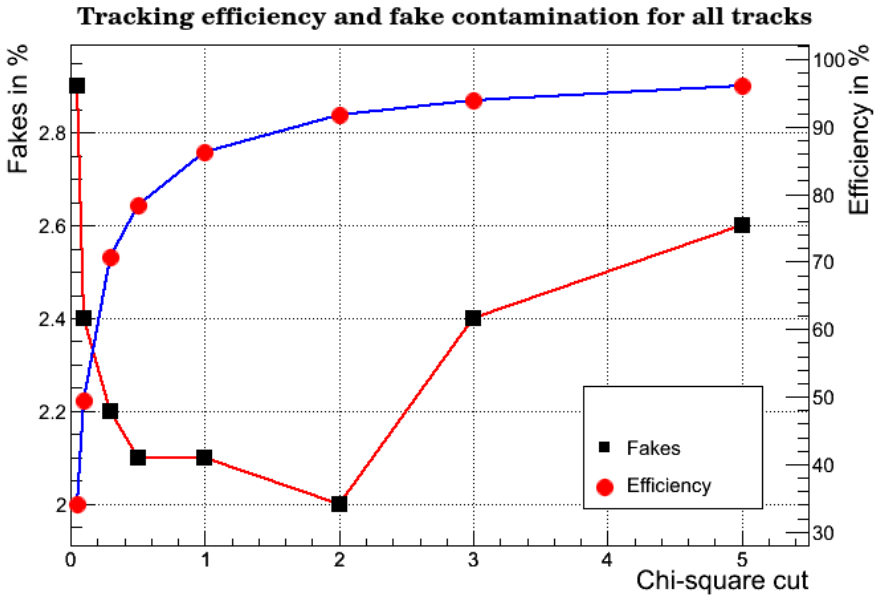


Figure 4.17: Tracking Efficiency and fake contamination as a function of $\chi^2$ cut for all reconstructed tracks.

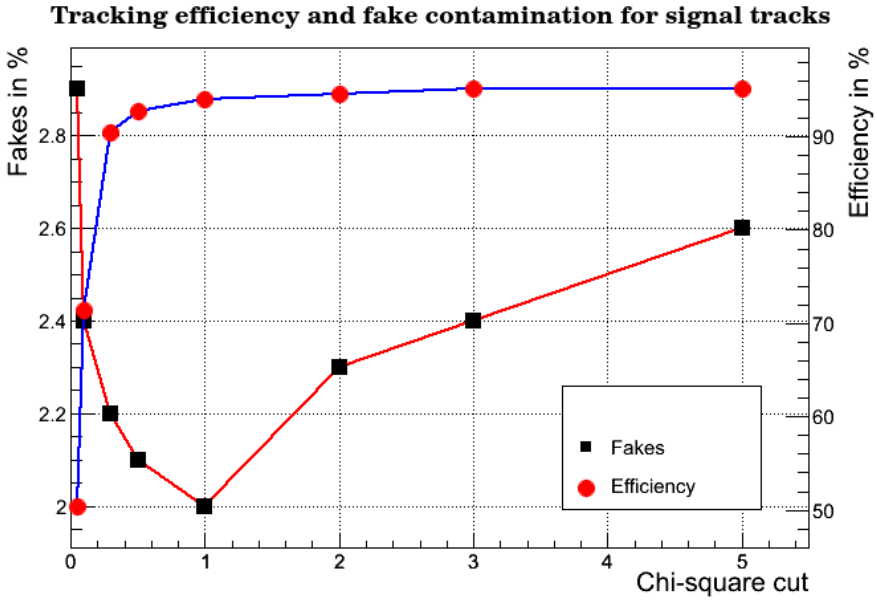


Figure 4.18: Tracking Efficiency and fake contamination as a function of $\chi^2$ cut for all signal tracks.

tion plotted as a function of a $\chi^2$ cut for all reconstructed tracks and signal tracks, respectively. The efficiency increases with the increasing value of $\chi^2$ cut. The average number of fakes is on the order of 2%. The efficiency of the signal tracks is almost

saturated at a $\chi^2$ cut value of 1.

### 4.3.5 Track position uncertainty

The primary GEANT track from the primary interaction point is extrapolated to each station and a corresponding associated uncertainty is determined for each VD station. These uncertainties are used for the weighted regression fit in the track extraction procedure. The uncertainty increases with the distance from the primary interaction position due to multiple scattering. Figure 4.19 shows the prepared fits for each station. The sigma value clearly shows the increase of uncertainty for each VD station. The deviation from the Gaussian distribution is due to the convolution of different particle momenta. We however did not apply momentum dependence analysis, thus the VD tracking does not rely on the momentum information.

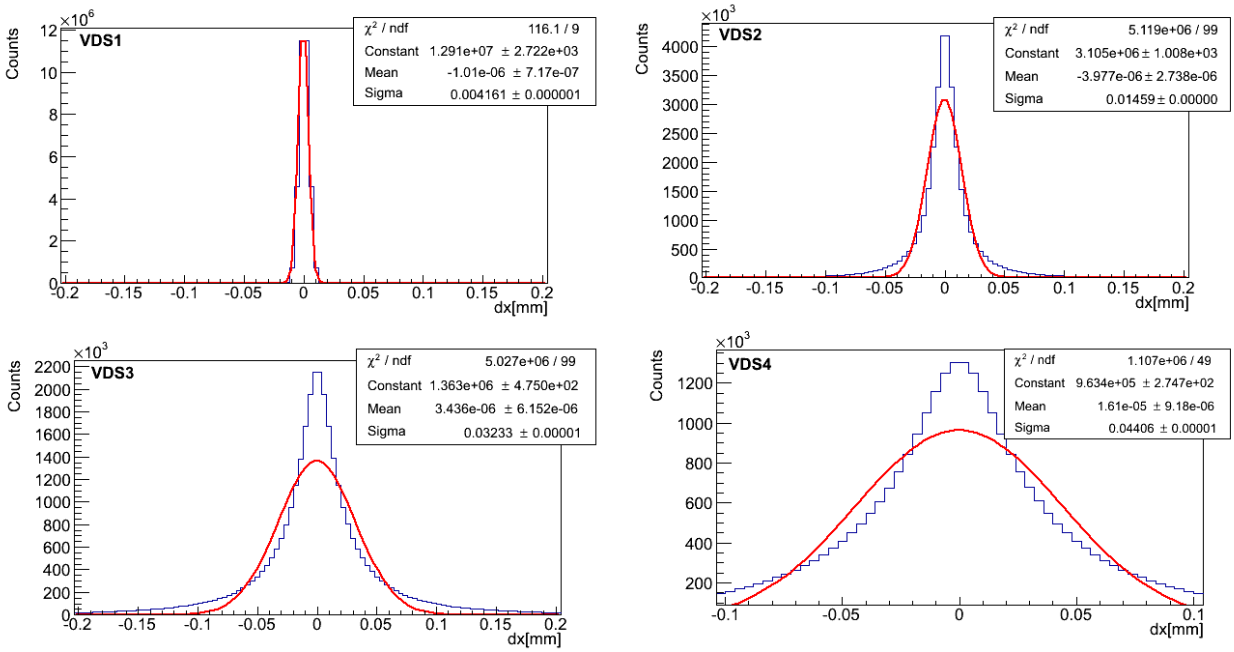


Figure 4.19: Uncertainity variation with the distance of station from the target position.

## 4.4 Analysis and background reduction

$D^0$ mesons decay at a distance of a few hundred microns from the interaction point. In order to select pion and kaon pairs that originate from the $D^0$ decay, the decay vertex needs to be reconstructed with a precision on the order of 10 $\mu$m. The vertex resolution of the present TPC based tracking system of the NA61/SHINE experiment is much worse than required for $D^0$ decay vertex reconstruction and identification. Thus, a high resolution VD is required which allows precise track reconstruction in the proximity of the target. Figure 4.20 shows the invariant mass distribution of pion-kaon pairs from central Pb+Pb collisions at 158A GeV. It is obvious that the background is higher by several orders of magnitude compared to the $D^0 + \overline{D}^0$ signal. In order to reduce the combinatorial background, four cuts were applied:

(i) cut on the track transverse momentum $p_T$,

(ii) cut on the track impact parameter $d$ ,

(iii) cut on the longitudinal position $V_z$ of the track pair vertex relative to the primary interaction point,

(iv) cut on the parent particle impact parameter $D$. .

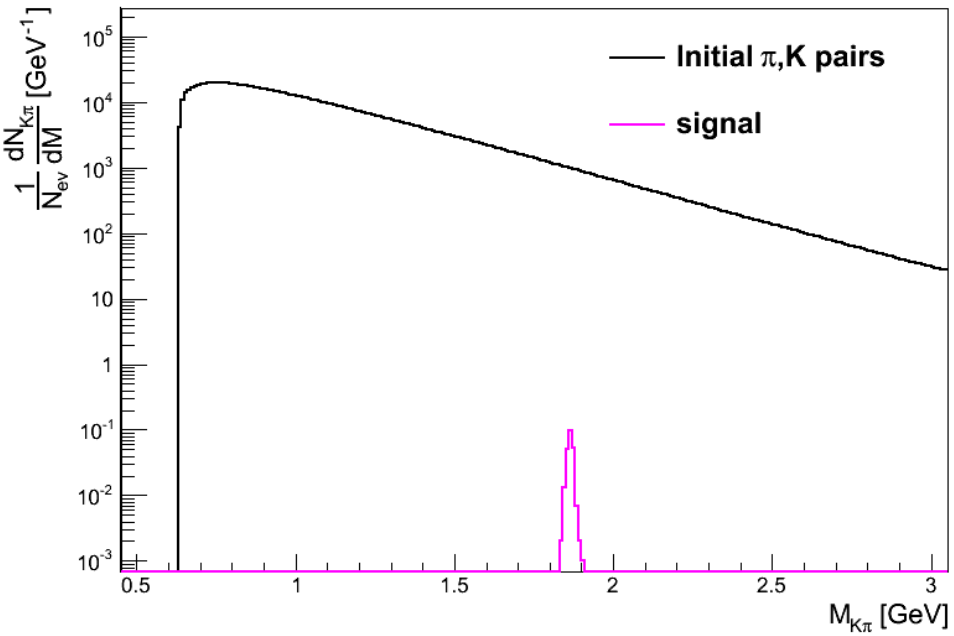


Figure 4.20: The invariant mass distribution of all pion-kaon pairs in central Pb+Pb collisions at 158A GeV with the $D^0$ signal at 1.86 GeV shown separately.

The first two are single-particle cuts, while the last two are two-particle cuts. It must be emphasized that the proposed VD will provide the required precise tracking information near the target for the cuts (ii)–(iv). The graphical definitions of the cut variables and their distributions are illustrated by Figures 4.21 and 4.22 respectively.

The transverse momentum distribution of signal and background tracks are shown in the top left diagram in Figure 4.22. The signal spectrum is shifted to higher values of $p_T$ compared to the background. Thus rejection of low $p_T$ tracks significantly reduce the background while the low fraction of the signal will be removed.

The track impact parameter $d$, the distance of the closest approach between the back-extrapolated track and the primary interaction vertex is defined in Figure 4.21 (a). The distributions of $d$ for background and signal tracks are depicted in Figure 4.22, top right. The spread of the $d \approx 0$ peak of the background is related to multiple scattering in the target and detector material as well as to limited detector resolution for the tracks originating from the primary interaction (thin gray/black

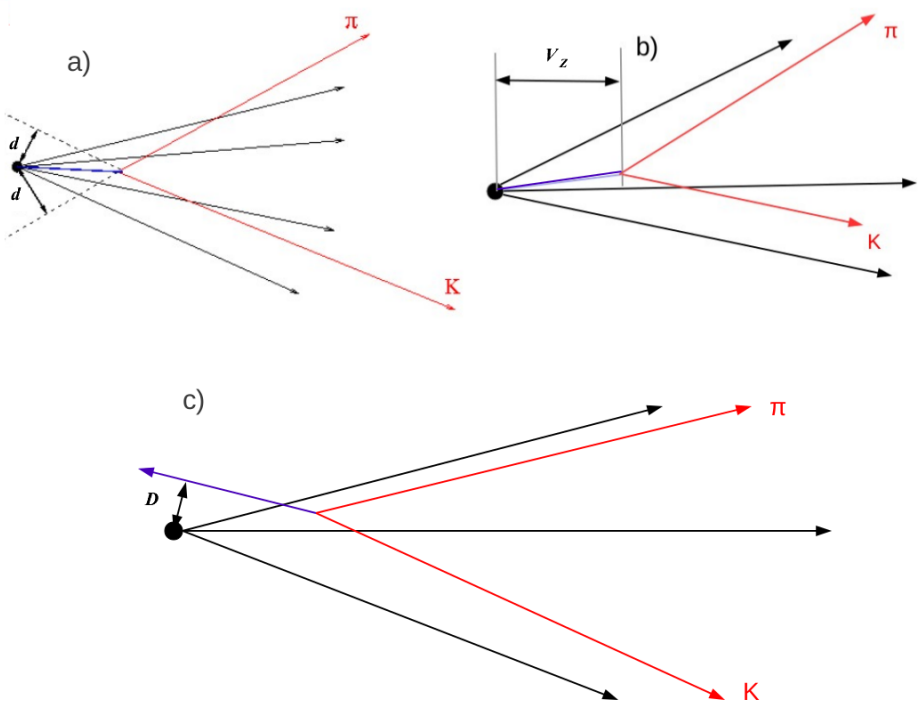


Figure 4.21: The Sketch of the decay topology withe the graphical definitions of the cut variables.

arrows). The displacement between the primary interaction point and the $D^0$ decay vertex results in a larger value of $d$ for tracks originating from decays of $D^0$s (red arrows). Rejection of tracks with small values of $d$ will remove mostly background.

$V_z$, the longitudinal position of the track pair vertex relative to the primary interaction point, is defined in Figure 4.21 (b). As can be seen in the bottom left plot in Figure 4.22, the $V_z$ distribution of the background peaks sharply around zero and gets the largest contribution from pairs of primary interaction tracks. This contribution can be largely removed by rejecting low $V_z$ pairs.

The parent particle impact parameter $D$ is the distance of closest approach between the primary interaction vertex and the reconstructed trajectory of the $D^0$ meson. Figure 4.21 (c) shows an example of the reconstructed trajectory of a $D^0$ (blue arrow) which decays into a measured pair of tracks (red arrows). Because $D^0$ originates from the primary interaction vertex moreover, for signal pairs the value

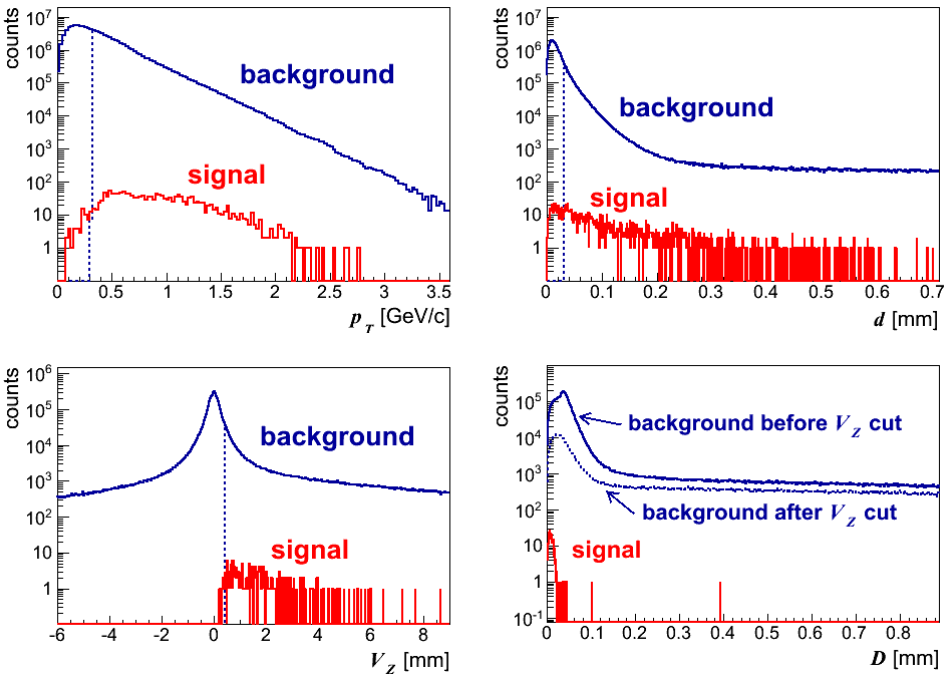


Figure 4.22: Distributions of $p_T$, $d$, $V_Z$ and $D$ variables for background (blue) and signal (red). For a description of the two background distributions for $D$ see the text. Dotted vertical lines show the optimized cut values.

of $D$ is peaked at zero, where it overlaps with small fraction of the background see Figure 4.22, bottom right. For the background pairs, which are located at $d$ are correlated with the peak at $V_z = 0$. This can be seen from Figure 4.22 which shows that by applying the $V_z$ cut, the background peak in the signal region of small $D$ values is reduced by the factor of 20. The long tail of the background is associated with pairs formed e.g. from a track that comes from the primary interaction point and another that originates from a decay. This tail can be removed by rejecting pairs with large $D$ values.

The cuts described above were optimized in order to obtain a maximum of the signal to noise ratio (SNR). The vertical lines in Figure 4.22 depict the optimal values of the cuts. In the further analysis, only tracks that satisfy the conditions $p_T > 0.4\,\mathrm{GeV}/c$ and $d > 40\,\mu\mathrm{m}$ as well as pairs of tracks that satisfy $V_z > 500\,\mu\mathrm{m}$ and $D < 22\,\mu\mathrm{m}$ are accepted.

Figure 4.23 shows the initial invariant mass distribution (black) in central Pb+Pb collisions at 158A GeV and the effect of subsequent application of the cuts: namely, after the cut on $p_T$ (magenta), cut on $p_T$ and $d$ (yellow), cut on $p_T$, $d$ and $V_z$ (blue) and finally cut on $p_T$, $d$, $V_z$ and $D$ (red). When the complete set of cuts is applied, the $D^0 + \overline{D}^0$ signal peak emerges at the $D^0$ invariant mass of 1.86 GeV. With the developed background reduction strategy the signal is suppressed by a factor of 1.8, while the background in the signal region is reduced by a factor of $10^6$.

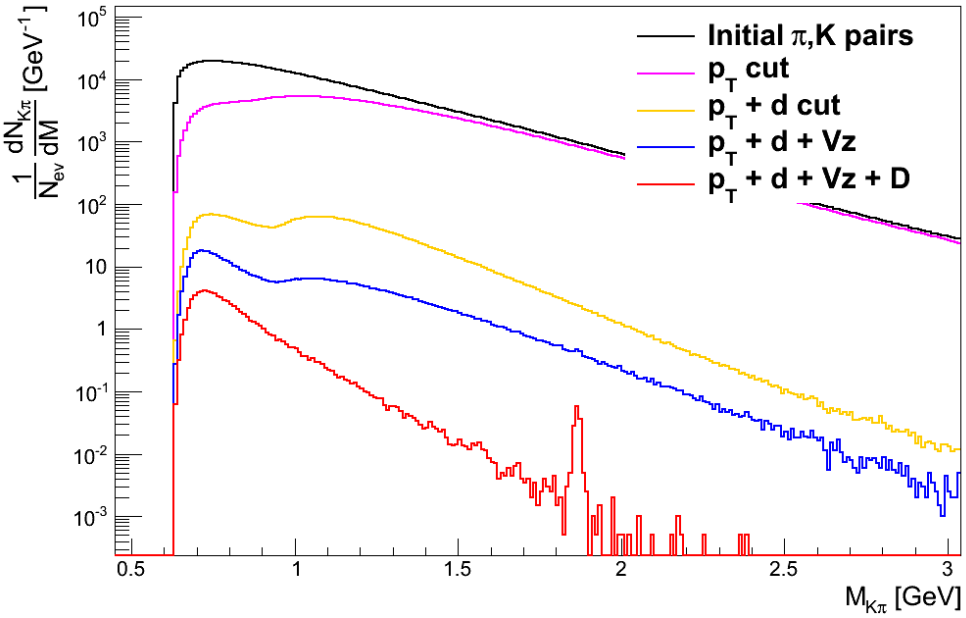


Figure 4.23: The invariant mass distribution for pion-kaon pairs for 200k central Pb+Pb collisions at 158A GeV. The $D^0 + \overline{D}^0$ open charm signal clearly emerges at 1.86 GeV with all cuts applied.

## 4.5 Technology of the Vertex Detector

The MIMOSA-26 [79] sensor has been selected as the basic detection element for the VD stations. MIMOSA-26 is basically a CMOS sensor whose architecture is based on MIMOSA-22 (Monolithic Active Pixel Sensor (MAPS) with fast binary readout). The floor view of the MIMOSA-26 sensor is depicted in Figure 4.24. This sensor is based on smaller feature size (0.35 $\mu$m) technology. The sensitive area of the

chip is about 1.06 × 2.12 $cm^2$. The sensor matrix is composed of 576 × 1152 pixels with a 18.4 $\mu$m pitch. The pixel design is based on self biased diode architecture. The thickness of the epitaxial layer is 14 $\mu$m. In MIMOSA-26 all the pixels in a row are read out simultaneously and the rows are read one by one in a rolling shutter mode. This approach leads to a readout time of 115.2 $\mu$s at an operation frequency of 80 MHz. Amplification and Correlated Double Sampling (CDS) units are included in each pixel. After analogue to digital conversion, digital signals pass through a zero suppression circuit and are then stored in memory. In order to perform read and write operations simultaneously, two memory banks are implemented in the sensor. As shown in Figure 4.24, an analogue output is implemented for test purposes on one side of the sensor (on the top). On the other side (the bottom part) of the sensor, the signal processing units are located.

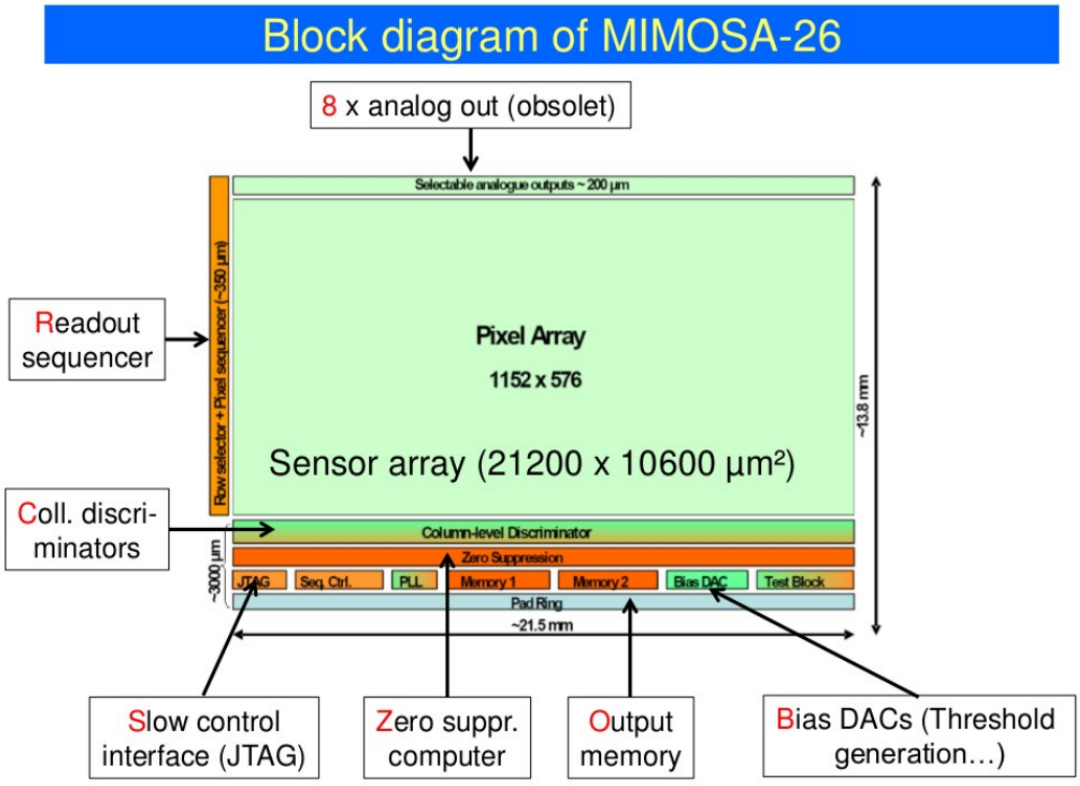


Figure 4.24: Schematic of the MIMOSA-26 chip showing the basic architecture.

In order to determine the requirements for the detector, a simulation framework was developed. The MIMOSA-26 was selected because of the expected very high hit occupancy of 5 hits/mm$^2$ /event in the inner region of the first VD station for central Pb+Pb collision at 158A GeV (see section Vertex detector occupancy). Such high hit occupancy cannot be handled by existing micro-pattern gas detector due to their one dimensional readout and with their accessible pitch size of 100 $\mu$m, they are not able to seperate two particles for the expected occupancy in the NA61/SHINE experiment. On the other hand, MIMOSA-26 provides two dimensional readout with high pixel granularity. MIMOSA-26 sensors can be reduce to 50 $\mu$m thickness which results in a small contribution of sensor to the material budget compared to the mechanical support, readout cables and cooling fluid. MIMOSA-26 is suitable for charged particle detection with hit density up to $10^6$/cm$^2$/s. Proton beam tests of MIMOSA-26 sensors proved that these devices can withstand fluences of up to $3 \times 10^{12}$ $n_{eq}$/cm$^2$ which provide a sufficient safety margin for use in NA61/SHINE [79] (see section Fluence estimates).

Table 4.2 shows a comparison of MIMOSA-26 technology performance with that of Hybrid and Charge-Coupled Device (CCD) technologies [80, 81]. It seems that only MIMOSA-26 can fulfill the requirements of the NA61/SHINE application and we use this device as the basic detection element of the VD stations.

Table 4.2: The NA61/SHINE requirements and limits for different chip technologies. (1) and (2) refer to non ionizing and ionizing doses respectively, per week of beam on target.

| | NA61 | Hybrid | CCD | MIMOSA-26 |
|---|---|---|---|---|
| Resolution. | $< 5\,\mu$m | $30\,\mu$m | $< 5\,\mu$m | $3.5\,\mu$m |
| Mat Budg. | $\sim$0.1% $X_o$ | $\sim$1% $X_o$ | $\sim$0.1% $X_o$ | 0.05% $X_o$ |
| Rad.Tol.(1) | $3 \times 10^{10}$ $n_{eq}$/cm$^2$ | $> 10^{14}$ $n_{eq}$/cm$^2$ | $< 10^9$ $n_{eq}$/cm$^2$ | $> 10^{13}$ $n_{eq}$/cm$^2$ |
| Rad.Tol.(2) | $\sim$1 krad | >10 Mrad | $\sim$1 Mrad | >300 krad |
| Time res. | $\sim 100\,\mu$s | 200 ns | $\sim 1000\,\mu$s | $115.20\,\mu$s |

# CHAPTER V

# Vertex Detector studies

## 5.1 Particle detection with silicon detectors

Silicon charged particle detectors are made from wafers of silicon having surface contacts forming a p-n junction. In order to fully deplete a detector a reverse bias voltage ($\approx$ 100 V) is applied. The electric field separates the charges (electron-hole pairs) produced by ionising radiation, and thus avoids recombination. Electrons drift toward the anode, while holes drift to the cathode. This collected charge produces a current pulse on the electrode, whose integral equals the total charge generated by the incident particle, i.e. it is a measure of the deposited energy.

Valence band free electrons can be excited to the conduction band by electromagnetic interaction or thermal excitation. Electromagnetic interactions can be caused, for example by photons with energy higher than $E_g$, the band gap (e.g.visible light), or by charged particles traversing the depletion region. Minimum ionizing particles excite roughly 80 electrons pairs per $\mu$m of particle trajectory. As electrons move towards the conduction band they leave behind holes, thus generating 80 electron hole pairs per $\mu$m of silicon. Besides the energy deposition due to charged particles it is important to describe the interaction of x-rays in silicon. These particles are typically absorbed and excite a fast primary electron. This electron is slowed down by exciting secondary electrons to the conduction band. The number of electron hole

pairs generated in this local interaction is given by equation 5.1 [82] below

$$N_{e^-} = \frac{E_{X-Ray}}{3.6\,eV} \qquad (5.1)$$

The free charge carriers generated by the radiation can be used to produce an electrical signal from the silicon detector. The corresponding current pulse can be directly detected which depends upon the detector material.

## 5.2 Pixel detector technologies

Traditionally hybrid and Charge Coupled Device (CCD) [80, 81] technologies are used in silicon pixel detectors. In hybrid pixel semiconductor detectors, the pixel sensors and the readout electronics are fabricated separately and then joined together by bump bonding (hence the name hybrid). The pixels can have a surface areas as small as $50 \times 50$ $\mu$m. Such devices provide spatial resolution of around $\approx 30$ $\mu$m, their radiation tolerance is on the order of $10^{14}$ $n_{eq}/cm^2$ [80, 81] and the time resolution (time precision with which the detector can identify a particle hit) is about 20 $\mu$s. However, due to bump bonding between sensor and front end chip the material budget is rather high.

CCDs are based on the principle of sideways depletion of a double diode structure. The charge is confined in a single well by potential barriers. The stored charge packets are subsequently transferred to the neighbouring column towards the readout electronics. CCDs provide very high granularity with pitch size on the order of 10 $\mu$m along with a large detector area. As they can be thinned down to a low material budget of $\approx 0.1\%$ $X_0$ (radiation length) they are an attractive solution for tracking devices. But on the other hand CCDs have a poor radiation tolerance $< 10^9$ $n_{eq}/cm^2$ because radiation induced defects trap charge during transfer.

## 5.3 Monolithic Active Pixel Sensors

Monolithic Active Pixel Sensors (MAPS) are low voltage CMOS sensors [83]. These sensors allow one to integrate the readout electronics and detector element on the same substrate. They are produced by a standard industrial process and hence are low cost devices. The technology provides a good compromise between rate capability and sensitivity. MAPS achieve very good spatial resolution on the order of $\approx 3.5$ $\mu$m. Their thickness can be reduced significantly below $\leq 0.05\%$ $X_0$ without any performance loss [84]. MAPS sensors can tolerate a non-ionizing radiation dose of about $10^{14}$ $n_{eq}/cm^2$. The cross-section of a MAPS device is shown in Figure 5.1.

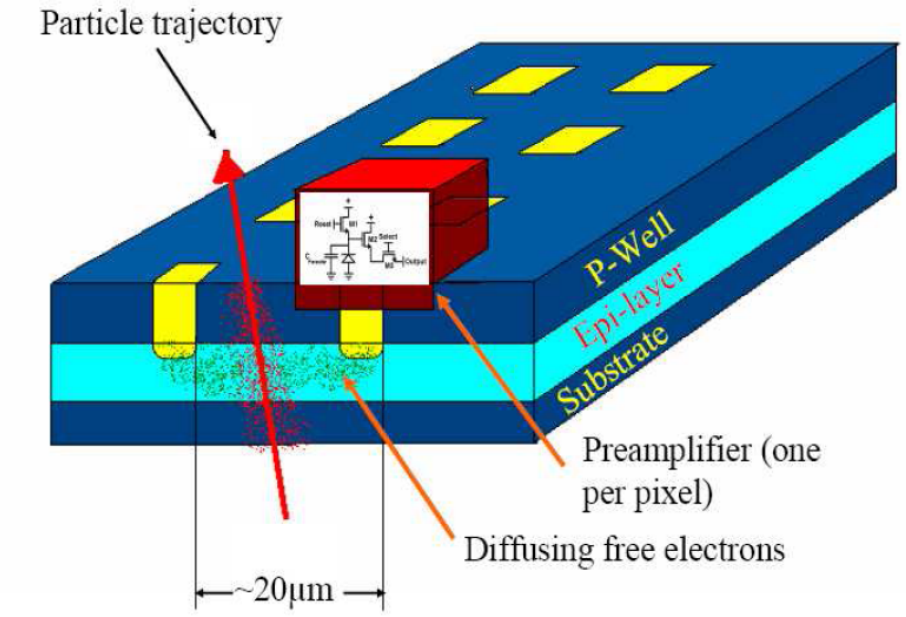


Figure 5.1: Schematic view of the cross section of a MAPS device [85]. The epitaxial layer is shown in cyan. The distance between collecting diodes is 20$\mu$m.

A MAPS sensor consists of three different P-doped silicon layers, i.e. the substrate, the P-well and a very thin moderately doped epitaxial layer which forms the sensitive volume of the device. This sensitive layer lies between the substrate and the P-well as shown in Figure 5.1. The doping levels of the substrate and the P-well are several orders of magnitude higher than that of the epitaxial layer. A minimum

ionizing particle (relativistic particle with charge z = ± e) produces excess carriers in the (low-resistivity) epitaxial layer at a rate of about 80 electron-hole pairs per $\mu$m particle trajectory in the volume.

The liberated electrons diffuse thermally inside the layer and are trapped due to the repulsive layer of P+/P- junctions [86]. The charge produced in the sensitive layer is collected by N-wells which are the charge collection diodes. The total thickness of the epitaxial layer is on the order of 10-20 $\mu$m and the charge collection time for a typical pixel pitch of 20 $\mu$m is about 100 ns. The charge is collected by thermal diffusion and possible distribution over a cluster of pixels.

### 5.3.1 Pixel readout

Conventional MAPS chips are designed as an array of pixels with the readout and processing electronics located at the periphery of the chip. Every pixel in the array is connected to an analogue output and can be accessed by selecting the row line by means of two shift registers. The pixels are read sequentially and will be referred to as serial readout. Their output signal is multiplexed and driven by an output amplifier to the outside world. Once all pixels in the matrix have been read out, the process re-starts from the first pixel. In general, the time resolution is equal to the readout time of a frame. A typical readout time for the serial readout approach is on the order of 1 ms. The time needed to read out a complete pixel matrix is obviously proportional to the time needed to read out an individual pixel and depends on the number of pixels in the matrix. A speed up can therefore be achieved by subdividing this matrix and performing the readout by several parallel output channels.

## 5.4 Development status of the MAPS sensors

The latest generations of the MAPS sensors include MIMOSA-25 [87] and MIMOSA-26 [79]. As the MIMOSA-26 sensor is selected as the basic detection unit for the future

vertex detector, its main features are summarized here. This sensor was fabricated with a technology that uses a feature size of 0.35 $\mu$m, smaller than in previous MAPS sensors. The chip features a sensitive area of about $1.06 \times 2.12\,\mathrm{cm}^2$ with the pixel pitch of 18.4 $\mu$m, resulting in $576 \times 1152 = 663.5k$ pixels per chip. In MIMOSA-26 all pixels in a row are read simultaneously and the rows are read one by one in a rolling shutter mode. With an operational frequency of 80 MHz the chip readout time is 115.2 $\mu$s. The device performs on chip data processing. Each pixel includes an amplification and Correlated Double Sampling (CDS) unit and each column end is equipped with a discriminator. After analogue to digital conversion, digital signals pass through zero suppression circuits. The digital signals are processed in parallel on 18 banks, then stored row by row in the memory. Two memory banks are implemented in the sensor to perform read and write operations simultaneously [79].

An important argument for selecting the MIMOSA-26 chip was that these sensors can be thinned to $50\,\mu$m thickness. This means that the sensor itself constitutes only a small fraction of the total material introduced by mechanical support, cooling fluid and readout cabling.

## 5.5 Detector response model

A detector response model developed for the Compressed Baryonic Matter (CBM) experiment [88] was evaluated for possible use in the present vertex detector study. The model consists of two important modules namely, Digitizer and Hit-Finder. These hardware related modules were adopted to the framework developed for the NA61/SHINE experiment. The digitizer simulates the signal charge integrated in different pixels starting from the traversal points of simulated tracks. It defines the trajectory of the particle in the detector as a straight line between the entry and exit point of the particle. Secondary particles produced within the station itself are ignored. The digitizer does not react to neutrons and gammas and also ignores the

contribution from nuclear fragments. It calculates the trajectory through the sensitive volume of the sensors which typically is much thinner than the station. It is assumed that the charge deposited by the incident particles in the epitaxial layer has a Landau-distribution.

The two kinds of digitizers commonly used to describe the charge transport through the MAPS sensors are the Lorentz and the Gauss digitizer. The digitizer used in the present simulation is the Lorentz digitizer which provides a good description of the diffusion process of charge in the undepleted MAPS. The algorithm uses a two dimensional Lorentz peak to distribute the charge of the individual segment onto the different pixels. On the other hand, the Gauss digitizer models the charge transport and diffusion in depleted sensors (like strip and hybrid-pixel detectors). It assumes that charge is dispersed by diffusion while collected by the depletion voltage of the sensor. The digitizer module generates the so-called digis that contain the charge in units of electrons.

### 5.5.1 Cluster simulation and reconstruction

The Hit-Finder module, as used in the present study, simulates the noise of the readout chain. It also offers the possibility to simulate fake hits. Due to the excessive CPU consumption this feature was not used. Based on the input from the digitizer module, the hit finder generates digitized hits representing data from the MIMOSA-26 sensors.

A charged particle passing through a MAPS detector generates an amount of charge which then diffuses in the sensitive volume until it is collected by several neighbouring diodes, forming thus a cluster of firing pixels. The reconstruction of the hit of the charged particle is based on the information provided by the cluster of pixels. First, the clusters of pixels are identified and next, the reconstruction of the impact point (hit) is performed. The reconstruction algorithm for clusters is based on

the signal-to-noise ratio (SNR) of the individual pixels given by the equation below:

$$SNR = \frac{S_k(n)}{n_k} \tag{5.2}$$

where $s_k(n)$ is the charge measured on the $k^{th}$ pixel of the $n^{th}$ event, and $n_k$ is the estimated random noise of the $k^{th}$ pixel. The signal-to-noise ratio is used because it allows to eliminate the so-called hot pixels showing high noise fluctuations but no significant signal charge. Once a seed pixel (pixel with highest signal to noise ratio) is identified, one defines the first, the second and the third pixel coronas around it as illustrated in Figure 5.2.

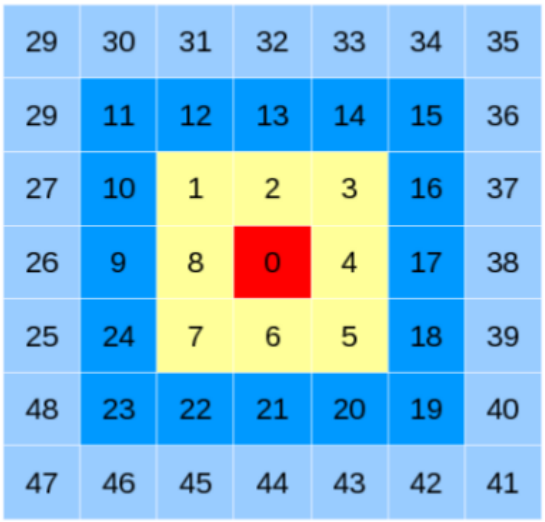


Figure 5.2: Depiction of the first (yellow), second (blue) and third (light blue) coronas around the seed pixel, shown in red.

The seed pixel has by definition the index 0. The first pixel corona is defined by the pixels with indices from i=1 to i=8, the second one has indices from i=9 to i=24 and the third one is defined by pixels from i=25 to i=48. Typical cluster sizes are geometrical regions of N = 5×5 or N =7×7 pixels. This is motivated by the observation that this number of pixels is sufficient to collect the diffusing charge. This group of pixels is now considered as a cluster candidate.

During the analysis it was observed that many clusters contain more than one seed pixel candidate. In order to avoid double counting, a seed pixel candidate, which is located in the accepted cluster of another seed pixel with higher SNR, is considered as neighbour of the latter. The candidate is therefore removed from the list of seed pixel candidates and cannot generate its own cluster. The cluster finding algorithm repeats the process until all clusters are identified. For all four VD stations the difference between x and y positions of the reconstructed hit and the original GEANT4 hit point are depicted in Figures 5.3 and 5.4 respectively.

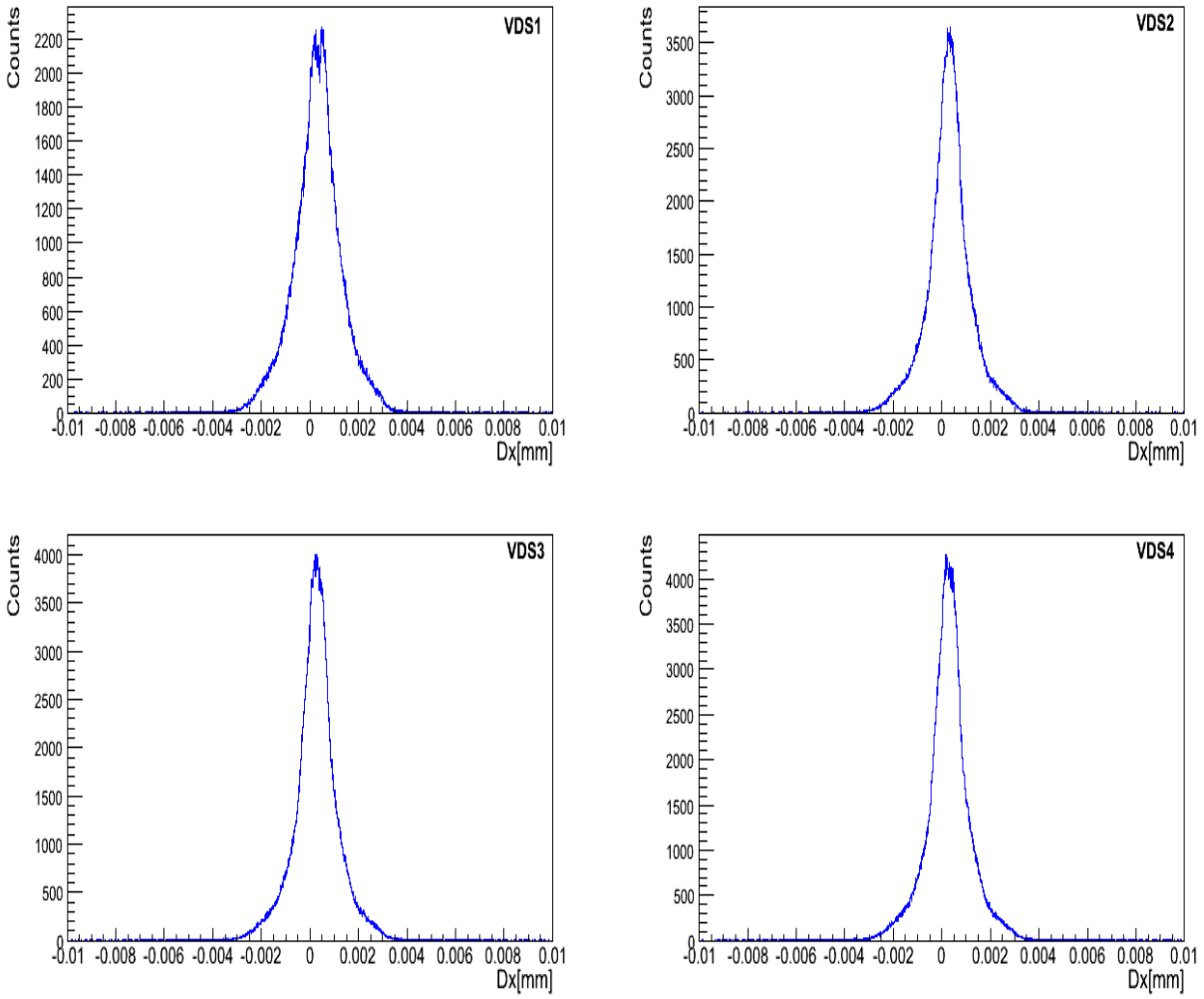


Figure 5.3: Difference of X position between reconstructed hit and GEANT hit (FWHM $\approx$ 2 $\mu$m ))

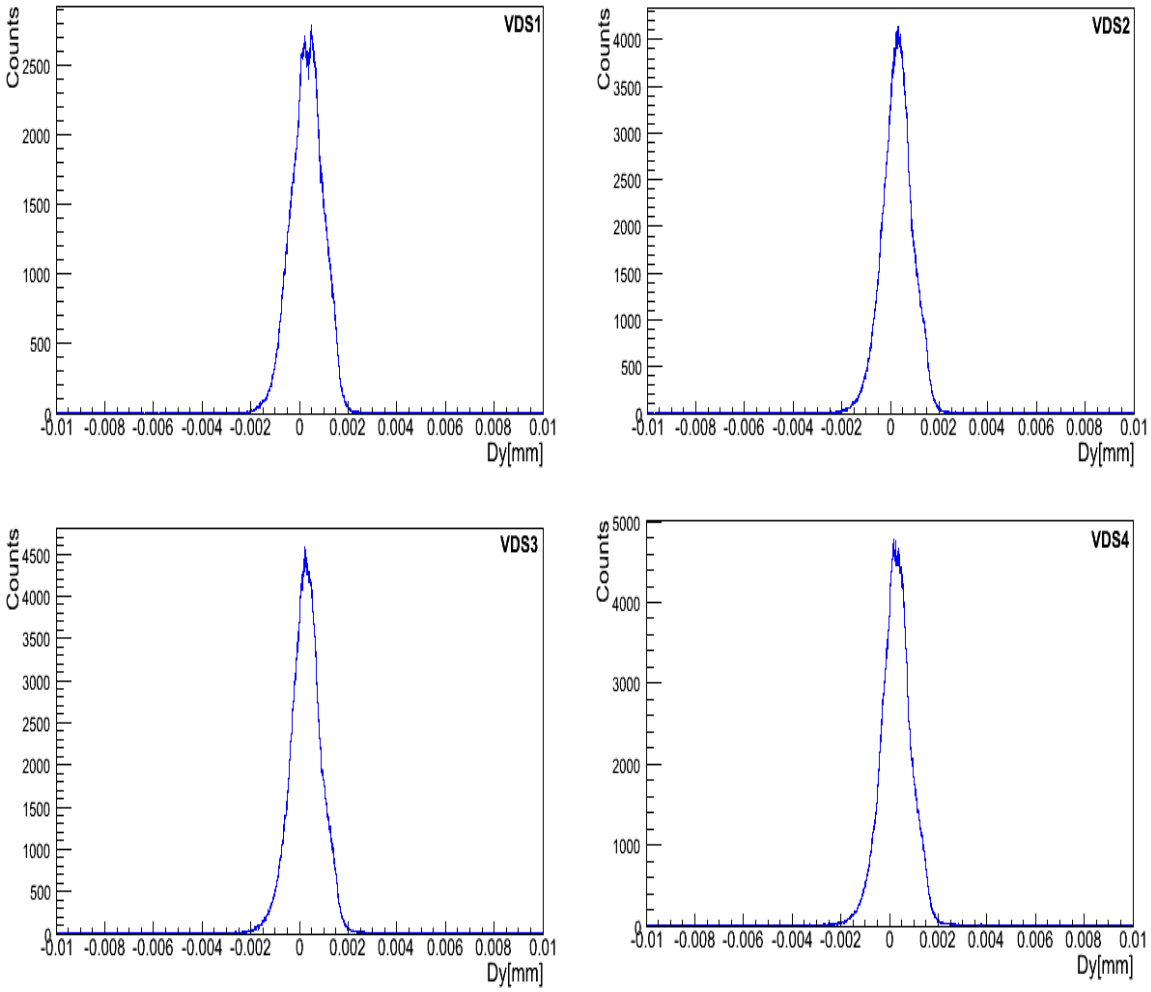


Figure 5.4: Difference of Y position between reconstructed hit and GEANT hit (FWHM $\approx$ 2 $\mu$m )).

The resolution obtained from the CBM sensor model is about 2 $\mu$m which is a too good spatial resolution compared to the value from the test measurements that is 3.5 $\mu$m [76]. In our vertex detector simulation we therefore did not employ the CBM detector response model. Instead applied smearing of GEANT hits position according to the uncertainty of 4 $\mu$m which is slightly larger than the experimental value.

# CHAPTER VI

# Results and discussion

## 6.1 Analysis results

The exact identification on a track by track basis is not possible in the whole phase space accepted by NA61/SHINE experiment. The analysis is done both with perfect particle identification (PID) and not utilizing the PID information, therfore the results are expected to lie between these two extremes. For the analysis assuming perfect PID, the species type is known for each track. The left panel of Figure 6.1 shows the invariant mass distribution with all the cuts applied and assuming perfect PID for Pb+Pb reaction at a collision energy of 158A GeV. The figure also depicts a fitted curve that represents a sum of exponential (background) and Gaussian (signal) functions. To calculate the yields of signal (S) and background (B) the distributions are interpreted over $\pm 3\sigma$ range around $D^0$ mass. This plot is compared to the one in the right panel of Figure. 6.1, which presents results of the analysis without utilizing the PID information. In this case for each unlike-sign pair of tracks, two hypothesis, corresponding to $D^0$ and $\overline{D^0}$, are tested — namely assuming that the negative track in the pair is kaon and the positive is pion and reversely. The comparison of the two plots shows that a much higher background is observed in the analysis without PID. Nevertheless, it is feasible to extract the signal yield even in such an analysis and the yield of $D^0$ and $\overline{D}^0$ is found to be consistent with that obtained in analyis that

assumes perfect PID.

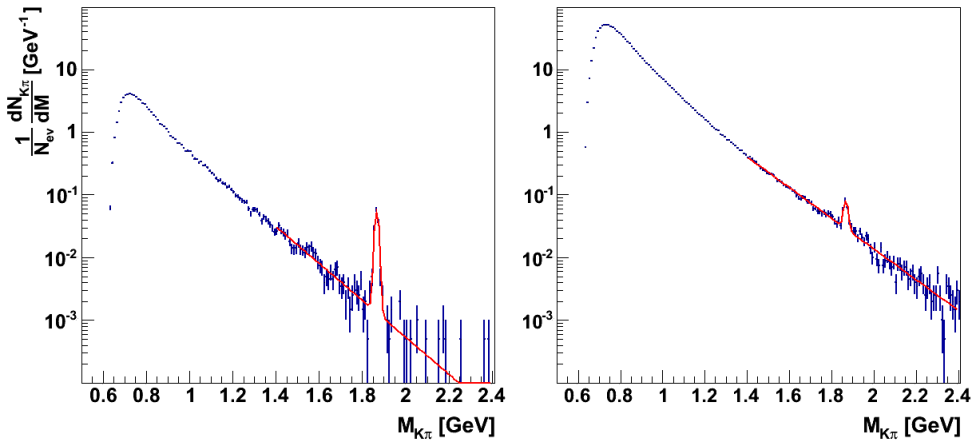


Figure 6.1: The invariant mass distribution of pion-kaon pairs after full background reduction for 200K central Pb+Pb collisions at a beam energy of 158A GeV. The red curve represents a fit with the sum of exponential (background) and Gaussian functions ($D^0$ signal). Left: analysis done using PID information. Right: analysis not utilizing the PID information (see text for more explanation). The $D^0 + \overline{D^0}$ signal peak emerges at $D^0$ invariant mass of 1.86 GeV.

The SNR and the total $D^0 + \overline{D^0}$ yield (S) are extrapolated to a sample of 50M central Pb+Pb events which is the anticipated event number collected during 1-2 months of NA61/SHINE data taking. For 158A GeV energy the total yield of $D^0 + \overline{D^0}$ is about 64k for the PID and no-PID case and the signal to noise ratio (SNR) ratios are 246 and 197, respectively.

Figure 6.2 presents the invariant mass distribution of pion-kaon pairs for Pb+Pb at the lower collision energy of 40A GeV with all the background reduction cuts applied. Only the analysis with PID is shown here. The total yield of $D^0 + \overline{D^0}$ is on the level of 2k for the PID and no-PID cases, and the corresponding SNR ratios are 11.3 and 2.1, respectively.

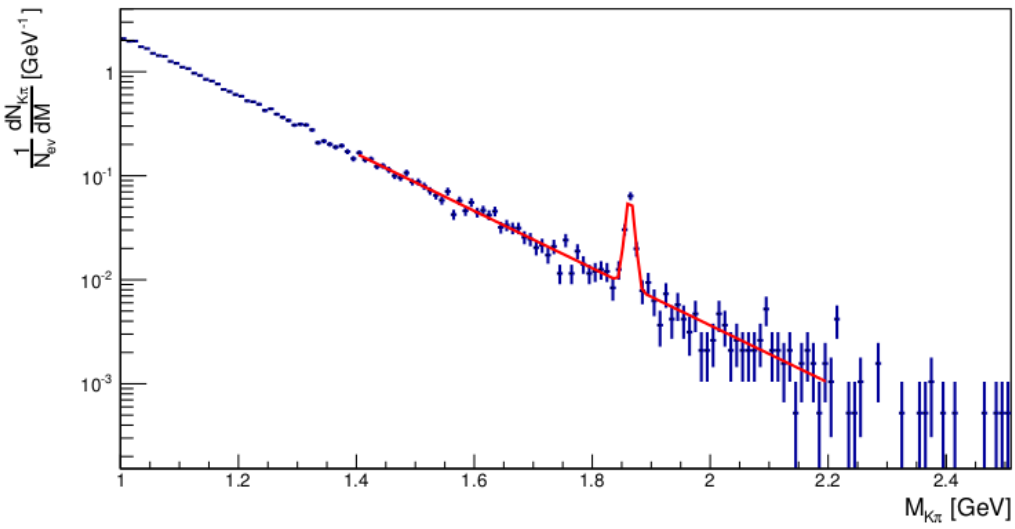


Figure 6.2: The invariant mass distribution of pion-kaon pairs after full background reduction for 200K central Pb+Pb collisions at a beam energy of 40A GeV. The red curve represents a fit with the sum of exponential (background) and Gaussian functions ($D^0$ signal). The $D^0$ peak is clearly visible at 1.86A GeV.

I have also performed the calculations for the lighter system of Ar+Ar collisions at a beam energy of 158A GeV. Figure 6.3 shows the invariant mass distributions of pion-kaon pairs for 500k events from 0-10% central Ar+Ar collisions at 158A GeV beam energy assuming perfect PID and no-PID scenarios. The cuts optimized for central Pb+Pb collisions at 158A GeV were applied. Again the yields were integrated over $\pm 3\sigma$ range around the $D^0$ mass and the SNR and the total $D^0 + \overline{D^0}$ yield (S) are extrapolated to a sample of 50M central Ar+Ar events. For analysis with and without PID, the total yield of $D^0 + \overline{D^0}$ is approximately 4k and the SNR ratios are equal to 67 and 3.2, respectively.

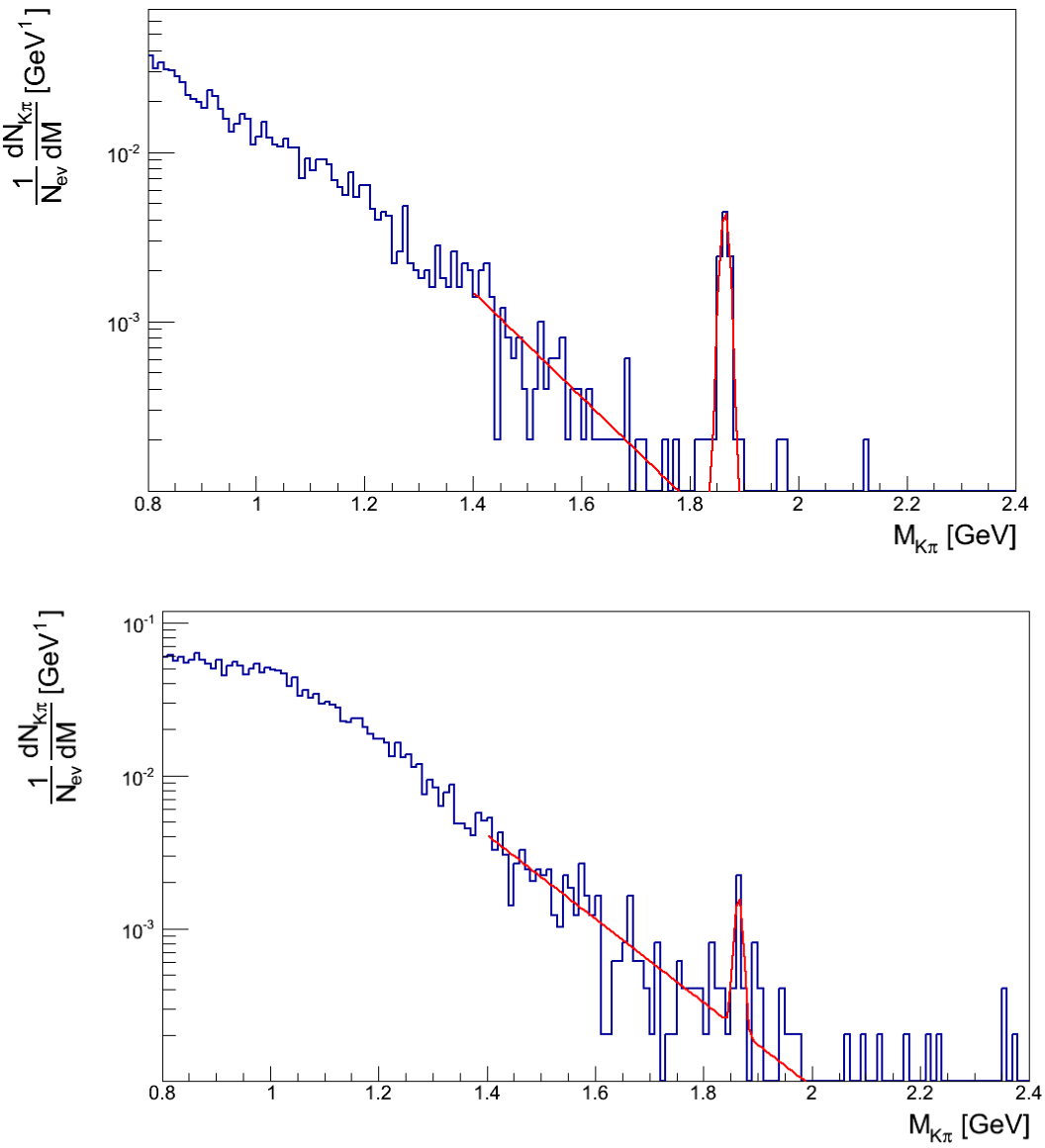


Figure 6.3: The invariant mass distribution of pion-kaon pairs after full background reduction for 500K central Ar+Ar collisions at a beam energy of 158A GeV. The red curve represents a fit with the sum of exponential (background) andGaussian functions ($D^0$ signal). Top: analysis using PID information. Bottom: analysis without utilizing the PID information.

The results obtained for open charm measurements at the top SPS energy of 158A GeV and the lower energy of 40ÅGeV for Pb+Pb reaction and at 158A GeV for Ar+Ar reaction, using the two analysis types – with and without PID – are summarized in Table 6.1. It is obvious from the table that the measurement of open

charm production seems to be feasible in the NA61/SHINE experiment at the top SPS energy of 158A GeV as well as at the lower energy of 40A GeV if the experiment is upgraded with the proposed vertex detector.

Table 6.1: Simulation results for the measurement of $D^0$ production in the decay channel $D^0 \rightarrow K^- + \pi^+$. The signal to noise ratio (SNR) and the total $D^0 + \overline{D}^0$ yield (S) are extrapolated to a sample of 50M central Pb+Pb events and Ar+Ar events.

| Reaction | Energy | 158A GeV | 158A GeV | 40A GeV | 40A GeV |
|---|---|---|---|---|---|
| | PID | perfect | no | perfect | no |
| Pb+Pb | S/B | 17 | 1.0 | 1.0 | 0.07 |
| | SNR | 246 | 197 | 11.3 | 2.1 |
| | S | 64k | 64k | 2k | 2k |
| | S/B | 23 | 1.9 | - | - |
| Ar+Ar | SNR | 67 | 3.2 | - | - |
| | S | 4k | 4k | - | - |

# CHAPTER VII

# Summary and conclusion

Direct measurements of hadrons containing charmed valence quarks provide important information about the initial stage of nucleus-nucleus collisions at relativistic energies. So far there is no direct measurement of the production of open charm hadrons at SPS energies whereas charmonium states $J/\psi, \psi, \chi$ have already been measured by the NA50/NA60 experiments in Pb+Pb and In+In reactions at 158A GeV.

This thesis presented a feasibility study of $D^0$ meson (open charm) measurements with the NA61/SHINE experiment at the CERN SPS. The measurements are challenging due to the low multiplicity and short life time of $D^0$ mesons. The decay path length of open charm hadrons is on the order of 100 $\mu$m. Thus in order to distinguish between the primary production and secondary decay vertex a high resolution VD is required. The design, geometry and detection technology for such a VD was discussed.

This study was done for the measurement of $D^0$ mesons via its decay into two daughter particles, $D^0 \rightarrow K^- + \pi^+$, in central Pb+Pb collisions at the top SPS energy of 158A GeV and the lower energy of 40A GeV, and for lighter system of Ar+Ar at 158A GeV. As physics input we generated 200k 0-10% most central collisions using AMPT event generator. It provides a good description of the background consisting of charged hadrons, mostly pions and kaons. The AMPT model predicts an average

multiplicity of 0.01 for $D^0+\overline{D}^0$ per central Pb+Pb event. This value seems to be underpredicted with respect to PYTHIA results for p+p collisions and scaled to number of binary nucleon-nucleon collisions in central Pb+Pb reactions (0.21) as well as with respect to the prediction of the HSD model (0.2). As the HSD model was tuned to properly describe available p+A and $\pi$+A charm production data at SPS energies, we scaled the AMPT multiplicities to the values predicted by the HSD model.

Within the 200k statistics, the AMPT event generator does not generate open charm at the lower energy of 40A GeV. However, we observed that the inverse slope parameter of the transverse mass distribution and the width of the rapidity distribution for kaons do not change by more than 10% from 158A GeV to 40A GeV. In order to describe the phase space for $D^0$ at the lower energy, we assumed changes in the transverse mass distributions similar to those observed for kaons. The total yield was taken as predicted by the HSD model.

We employed GEANT4 to describe particle transport through the NA61/SHINE experimental setup supplemented with a VD to allow precise tracking in the proximity of the target.

Our simulation shows that the combinatorial background under the $D^0+\overline{D}^0$ peak in the invariant mass distribution for kaon-pion pairs is much higher than the signal. Thus in order to extract the signal, we had to suppress the large combinatorial background. For this purpose we developed so called background suppression cuts applied to both single particles and particle pairs as described in detail in chapter 4.

The event reconstruction uses information on the hits in the VD stations as well as the track information from the current NA61 setup. Only the tracks which are accepted in the VTPC's are considered, namely we require, that the track length in the active area of VTPC1 and VTPC2 must be greater than 80 cm. Values found by the NA49 experiment for VTPC's momentum and position resolution are used. For

the VD simulation we used a position resolution of about 4 $\mu$m. The realistic track reconstruction is done based on the Hough Transform method. The tracks from the VD were extrapolated to the front of the VTPC for matching with the VTPCs tracks.

By using the developed simulation framework we were able to determine the requirements for the VD in terms of radiation tolerance, spatial resolution, material budget, readout speed and hit occupancy. Our simulation results show that the hit occupancy in the first station of the VD generated by a single central Pb+Pb collision at the top SPS energy of 158A GeV reaches a value of about 5 hits/mm$^2$/event in the innermost part of the detector. Such a high occupancy cannot be handled by existing micro-pattern gas detectors mostly because of their one-dimensional readout even for a hardly achievable strip pitch size on the order of 100 $\mu$m. Thus the MIMOSA-26 sensor whose architecture is based on the Monolithic Active Pixel Sensor (MAPS) with fast binary readout was chosen as a basic detection element of the VD stations. The size of the chip is 13.7 mm x 21.5 mm and the sensor matrix is composed of 576×1152 pixels with 18.4 $\mu$m pitch. This device is suitable for charged particle detection with a flux of up to $10^4$ hits/mm$^2$/s and provides a resolution of 3.5 $\mu$m in both orthogonal directions. The sensor is 50 $\mu$m thick and the total thickness of the detector is on the order of 0.3% $X_0$.

During the experiment, the VD is expected to be exposed to a high dose of radiation which can degrade the sensor performance. Based on the anticipated beam intensity and the interaction rates, the particle flux through the VD was calculated. Integrating the flux over 1 month (in 1-2 months NA61/SHINE can collect about 50M central Pb+Pb events) and using the so-called displacement damage function, fluences on the order of $2.6 \times 10^{10}\,n_{eq}/cm^2$ and $4.2 \times 10^{10}\,n_{eq}/cm^2$ were estimated in the most illuminated area of the sensors for $\delta-$electrons and hadrons, respectively. Tests of MIMOSA-26 sensors in a proton beam proved that these devices can handle fluences up to $3 \times 10^{12}\,n_{eq}/cm^2$ thus providing a large safety margin for using them

in the NA61/SHINE application.

The analysis is done both with perfect particle identification (PID) and without PID. The yield of $D^0$ and $\overline{D}^0$ is found to be consistent with that obtained using PID. For Pb+Pb collisions at 158A GeV energy the total yield of $D^0$+$\overline{D}^0$ is on the order of 64k for the PID and no-PID cases and at the lower energy of 40A GeV the total yield of $D^0$+$\overline{D}^0$ is on the order of 2k for the PID and no-PID cases respectively. In case of Ar+Ar reaction at 158A GeV for analysis with and without PID,the total yield of $D^0$+$\overline{D}^0$ is on the order of 4k. Thus from the analysis of simulated events, we find that the extraction of the $D^0$+$\overline{D}^0$ signal seems to be possible at the top SPS energy of 158A GeV as well as at the lower energy of 40A GeV. The Monte Carlo simulation results show that open charm measurements are feasible with the NA61/SHINE experiment, if it is supplemented with a new, high precision, VD.

This Thesis reports on the technical work motivated by the future experimental program of the NA61/SHINE Collaboration at the CERN SPS. This work is supported by the Foundation for Polish Science — MPD program, co-financed by the European Union within the European Regional Development Fund and the National Science Centre of Poland, grant UMO-2012/04/M/ST2/00816.

# APPENDIX

# APPENDIX A

# Radiation damage in silicon detectors

## A.1 Fundamental radiation effects

Silicon detectors are widely used in a hostile radiation environment. This radiation exposure not only results in the damage of the detectors but also has consequences for the operation of the device. The radiation damage mechanism in silicon is divided into surface damage and bulk damage, which are caused by two interaction chains resulting from ionizing and non-ionizing radiation. The ionizing radiation deposits energy into the electron gas of the material. This interaction destroys the chemical bindings but does not harm the silicon crystal as atoms keep their position in the crystal. The irreversible damage caused by this radiation is at the interface between silicon and $SiO_2$ (silicon dioxide). $SiO_2$ is the most commonly used insulator in micro circuits. These two materials have different lattice constants resulting in the formation of irregular bonds at the interface. Ionizing radiation breaks these bonds and hence modifies the electrical properties of the material. Damage occuring at the interface it is referred to as surface damage. Non-ionizing radiation causes bulk damage by creating defect states in the band gap of the silicon structures. Like impurities these

defects degrade the properties of the bulk silicon. Non-ionizing radiation can also knock out atoms from the crystal lattice. This type of damage is mostly caused by neutrons, while electrons and photons can not reach the momentum transfer required for displacing an atom. So the latter cause mainly ionization damage.

### A.1.1 Ionizing radiation

Ionizing radiation damage is caused by charged particles and photons with energy higher than that of UV-light. The SI-unit of ionizing radiation is Gray ($G_y$ = 1 J/$K_g$). Ionizing Energy Loss causes surface damage due to the accumulation of positive charges in the oxide ($SiO_2$) and at the Si/$SiO_2$ interface. Ionization in the oxide, however, is not fully reversible and may cause steady changes of the interface properties.

The ionizing particles can create electron/hole pairs in $SiO_2$ even though this material has a high band gap (8.8 eV ). These pairs created in the oxide either recombine or move in the case of an applied electric field. The mobility of the conducting electrons is substantially higher than that of the holes and thus without recombination they escape towards the neighboring conducting structures. Because of a lack of thermal electrons in the conducting band, the holes cannot recombine and diffuse to the opposite border of the $SiO_2$. With a certain probability, they are trapped by defect states present in the transition zone between $SiO_2$ and silicon before they can accept an electron from the semiconductor. The number of trapped holes, which at room temperature keep their positive charge, is limited by the number of corresponding precursors to a surface density of $Q_{sat} \approx 3 \times 10^{12}$ cm$^{-2}$ [89]. The defects generated by ionizing radiation can be repaired with hydrogen in an annealing process.

### A.1.2 Non-ionizing radiation and the NIEL-model

Non-ionizing radiation has small impact on the region between silicon and $SiO_2$ which is full of lattice imperfections due to the different lattice constants of the two materials. However this radiation mostly causes bulk damage in the sensor material which is one of the factors limiting the use of silicon detectors in the high radiation environment of high energy physics experiments. The bulk damage is caused by high energy particles (hadrons, leptons, photons) which displace atoms from their lattice site. The resulting silicon interstitial and left over vacancy (Frankel pair) migrate through the silicon and finally form the point defects. If the energy transferred to the first atom is high enough, a cascade of further displacements, which is referred to as a defect cluster.

The energy required to remove an atom from the lattice site depends upon the direction of the recoil of the atomic nucleus with respect to the crystal lattice. For silicon the mean threshold energy is on the order of 25 eV [89]. About 190 eV kinetic energy is required to displace an atom with protons or neutrons while for electrons the minimum kinetic energy is about 260 KeV due to their lower rest mass. A minimum energy of 15 KeV and 4.6 MeV is required for protons/neutrons and electrons respectively for generating defect clusters.

The semi-empirical Non Ionizing Energy Loss (NIEL) [91, 92] model describes how the radiation damage produced by different particles with different energies can be scaled. The NIEL hypothesis assumes that any displacement damage induced change in the material scales linearly with the amount of energy used in displacing collisions. In this model there is no absolute unit for the deposited energy, rather this energy is normalized to the energy deposition of a reference particle which is a 1 MeV reactor neutron. Thus the non-ionizing dose is given in units of $n_{eq}/cm^2$, the energy deposition of 1 MeV neutron penetrating $1\,cm^2$ of the detector surface. The non-ionizing dose generates primary vacancies and interstitials in the crystals which

create defect states in the band gap. These act as generation and recombination centres which ease thermal generation of minority carriers and increase the leakage currents in the collection diodes of the silicon detectors. Figure A.1 shows the NIEL factors of different particles as a function of their energy normalized to a 1 MeV neutron. The neutron equivalence is given by

$$\phi_{eq} 1MeV = \chi\phi \qquad \text{(A.1)}$$

where $\chi = 0.62/5$ for electrons and 0.62 for particles from hadronic interactions from Figure A.1.

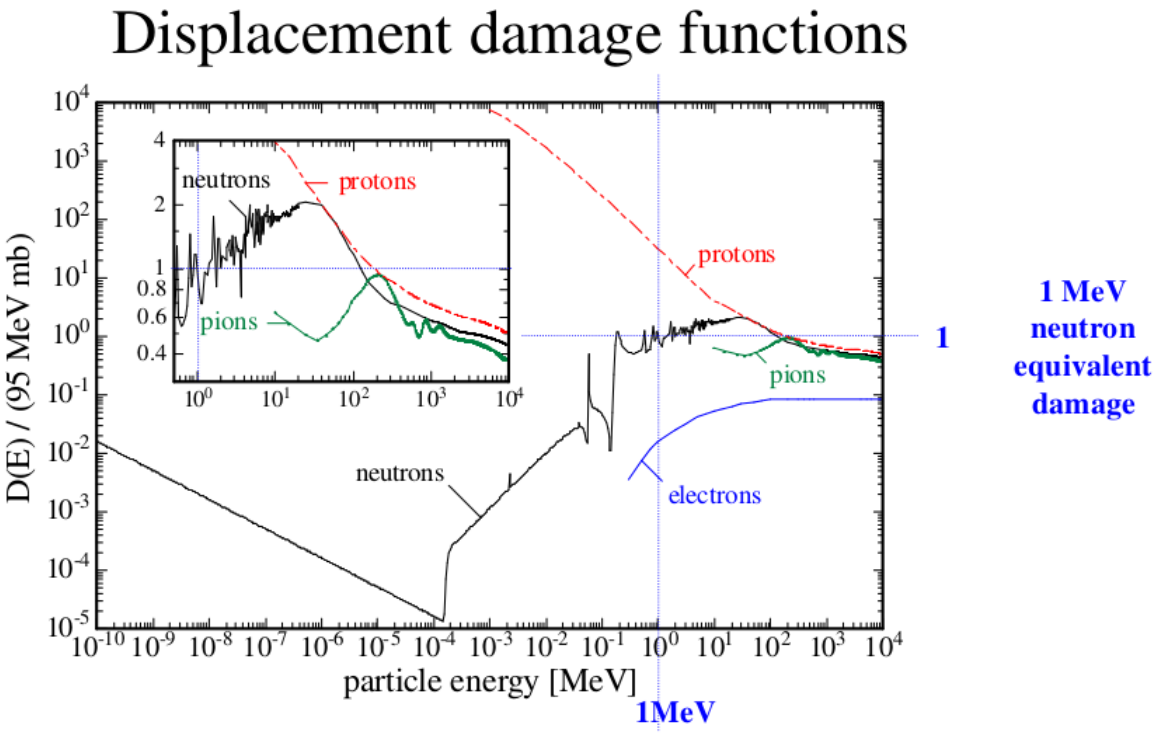


Figure A.1: Displacement damage function D(E) normalized to 95 MeV mb neutrons, as a function of particle energy. The factors are normalized to 1 MeV neutron equivalent. This figure is taken from [90].

The primary defects are not fixed in the material but diffuse in the detector material at room temperature resulting in some desired and undesired implications.

This diffusion of defects could result in the regeneration of the crystal lattice upon interstitial atoms filling a vacancy or moving to the edge of the crystal. In both cases, the defect is cured and the phenomenon is termed as beneficial annealing. On the other hand, if the outcome of the diffusion is more defects, like two vacancies or a vacancy and an oxygen atom bound with each other, the process is called reverse annealing. This causes much more damage to the detector than the primary defects. These defects increase the leakage current which, however, can be reduced by cooling.

# BIBLIOGRAPHY

# BIBLIOGRAPHY


[1] P. Braun-Munzinger, Nucl. Phys.**A 681** 119 (2001).

[2] D. J. Gross and F. Wilczek, Ultraviolet behavior of non-abelian gauge theories, Phys. Rev. Lett. **30,** 13431346, (1973).

[3] H. D. Politzer, Reliable perturbative results for strong interactions, Phys. Rev. Lett. **30,** 13461349, (1973).

[4] CTEQ Collaboration, R. Brock et al., Handbook of perturbative QCD: Version 1.0, Rev. Mod. Phys. **67,** 157248, (1995).

[5] K. G. Wilson, Confinement of quarks, Phys. Rev. **D10,** 24452459, (1974).

[6] E.V Shuryak, Phys. Rept. 61, 71 (1980).

[7] F. Karsch, Lect. Notes Phys. **583,** 209 (2002) [arXiv:hep-lat/0106019].

[8] O. Philipsen, Prog. Part. Nucl. Phys. **70,** 55 (2013).

[9] P. Braun-Munzinger et al., Phys. Lett. B **465** 15 (1999).

[10] J. Cleymans and K. Redlich, Phys. Rev. Lett.**81** 5284 (1998).

[11] R. Stock, Phys. Lett. B456 277 (1999).

[12] Investigation of Hadronic Resonances with STAR, Dissertation thesis, Yale (2006).

[13] W. Broniowski, W. Florkowski Phys Rev Lett. **87,** 27 (2001).

[14] W. Broniowski, W. Florkowski [arXiv:nucl-th/0112043v3] (2002).

[15] W.J. Willis, Conference On High-Energy Physics. 6-13 Sep, 1972, Batavia, Illinois.

[16] P.J.E. Peebles, THE STANDARD COSMOLOGICAL MODEL, Joseph Henry Laboratories Princeton University, Princeton, NJ, USA.

[17] D. Sticlet, Phase Transitions in the Early Universe Electroweak and QCD Phase Transitions Master Program of Theoretical Physics.

[18] Relativistic heavy-ion physics, CERN, arXiv:1010.3164[nucl-th].

[19] Y.Mehtar-Tani1, G.Wolschin International Symposium on Multiparticle Dynamics, DOI: http://dx.doi.org/10.5689/UA-PROC-2010-09/51 (2010).

[20] R. Singh, L. Kumar, P. K. Netrakanti and B. Mohanty, arXiv:1304.2969 [nucl-ex].

[21] M. Gyulassy and L. McLerran, Nucl. Phys. **A 750,** 30 (2005).

[22] K. Adcox et al. [PHENIX Collaboration], Nucl. Phys. **A 757,** 184 (2005).

[23] J. Adams et al. [STAR Collaboration], Nucl. Phys. **A 757,** 102 (2005).

[24] J. Takahashi, CERN Latin-American School of High Energy Physics (2011).

[25] F. Becattini et al. arXiv:hep-ph/0508188v2 21 Oct (2005).

[26] C Quintans et al, J. Phys. Conf. Ser. **50,** 353,(2006).

[27] O.Linyk et al., International Journal of Modern Physics E *arXiv:0808.1504v1 [nucl-th]* (2008).

[28] *The NA61/SHINE homepage.* [http://na61.web.cern.ch].

[29] T.Yao et al., 0809.0049v2 [nucl-th] (2009).

[30] M.Gazdzicki, C. Markert, Acta. Phy. Pol. B. No.4, **Vol 31,** (2000).

[31] T.Matsui and H.Satz,. Phys. Lett. **B 178,** 416, (1986).

[32] R.Vogt, . http://hips.web.cern.ch/HIPS/charm/dec99/vogt/ (1999).

[33] J. Aichelin,. http://hips.web.cern.ch/HIPS/charm/dec99/aichelin/ (1999).

[34] M. Gadzicki and M.I. Gorenstein,. Acta. Phys. Pol. **B 30,** 2705, (1999).

[35] M.I. Gorenstein,. Phys. Rev. **C 60,** 054903, (1999).

[36] H.Satz, *arXiv:hep-ph/0007069*, (2000).

[37] E.Cassing, L. Bratkovskaya, Phys. Rep. 308, 65 (1999).

[38] A.Capella, E.G.Ferreiro, A.B.Kaidalov Phys. Rev Lett. 85, **2018,** (2000).

[39] W. Cassing, E.L Bratkovskaya, A. Sibirtsev, Nucl. Phys.**A 691**, 753, (2001).

[40] E.Scomparina. (NA60 collab .), Recent results from the NA60 experiment (2009).

[41] U. Heinz, Nucl. Phys **A 661,** 140c (1999).

[42] H.Satz,. Progr. Rep. 310, **197** (1999).

[43] M.Masera, (NA50 Collab. ), J. Phys. G: Part.Phys. **27,** 667 (2001).

[44] R.Arnaldi et al., (NA60 Collab .), arXiv:0810.3204v2 [nucl-ex] (2008).

[45] H.Satz, BI-TP 2013/06, *arXiv:1303.3493v2 [hep-ph],* (2013).

[46] A. Adare et al., (PHENIX Collab .), Phys. Rev **C 84,** 044905, (2011).

[47] A. Adare et al., (PHENIX Collab .), Phys. Rev Lett**84,** 232301, (2007).

[48] L.Adamczyk et al., (STAR Collab .), *arXiv:1208.2736[nucl-ex]* (2014).

[49] S.Murphy Journal of Physics: Conference Series 375 042071 (2012).

[50] T.Czopowicz, (NA61 Collab. ) Status and Plans of the NA61/SHINE physics program, ISMD Conference (2011).

[51] Official CERNs web page. http://public.web.cern.ch/public/.13.

[52] S.Afanasiev et al., NIM **A430,** 210 (1999).

[53] D. Varga Study of inclusive and correlated particle production in elementary hadronic interactions, PhD Thesis, Budapest (2003).

[54] Umarov, Sabir; Tsallis, "On a q-Central Limit Theorem Consistent with Nonextensive Statistical Mechanics" Constantino and Steinberg, Stanly (2008).

[55] N. Agrball et al., Facility Paper JINST doi:10.1088/1748-0221/9/06/P06005 (2014).

[56] Zi-Wei Lin et al., Phy Rev. **C72,** 064901 (2005).

[57] P.Braun-Munzinger, J.Stachel, Phy, Lett B **490,** 196, (2000).

[58] Amsler C et al., (Particle Data Group) Phys Lett B **667**. 1,2008 and 2009 partial update for 2010 edition.

[59] P. Braun-Munzinger, J. Stachel, J. P. Wessels, and N. Xu, Phys, Lett B **344, 43** (1995).

[60] J. Cleymans andK. Redlich, Phys. Rev. Lett. **81,** 5284 (1998).

[61] C. M. Hung and E. V. Shuryak, Phys. Rev. Lett.**75,** 4003 (1995).

[62] D. H. Rischke, S. Bernard, and J. A. Maruhn, Nucl. Phys.**A595,** 346 (1995).

[63] H. Sorge, H. Stocker, and W. Greiner, Nucl. Phys. A498, **567C,** (1989).

[64] Y. Pang, T. J. Schlagel, and S. H. Kahana, Phys. Rev. Lett. 68, **2743,** (1992).

[65] B. Zhang,C.M.Ko, B. A. Li, and Z. W. Lin, in Atlanta 1999, Heavy Ion Physics from Bevalac to RHIC, edited by R. Seto (World Scientific, Singapore, 1999), p. 146.

[66] B. Zhang, C. M. Ko, B. A. Li, and Z. W. Lin, Phys. Rev. C **61,** 067901 (2000).

[67] X. N. Wang, Phys. Rev. D **43,** 104 (1991).

[68] X. N.Wang and M. Gyulassy, Phys. Rev. D **44,** 3501 (1991).

[69] B. Zhang, Comput. Phys. Commun. **109,** 193 (1998).

[70] B. Andersson, G. Gustafson, and B. Soderberg, Z. Phys. C **20,** 317 (1983).

[71] B. Andersson, G. Gustafson, G. Ingelman, and T. Sjostrand, Phys. Rep. **97,** 31 (1983).

[72] B. A. Li and C. M. Ko, Phys. Rev. C **52,** 2037 (1995).

[73] H. Appelshauser et al., (NA49Collaboration), Phys. Rev. Lett.**82,** 2471 (1999).

[74] J. Bachler et al., (NA49 Collaboration), Nucl. Phys. **A661,** 45, (1999).

[75] M. Winter for the IPHC team IPHC, Strasbourg, France CBM Progress report (2012).

[76] J. Baudit at al., "First test results of MIMOSA-26..", IEEE Nuclear Science Symposium, Orlando, USA (2009).

[77] Hough P.V.C., Method and means for recognizing complex patterns, U.S. Patent 3,069,654. Dec. (1962).

[78] Duda R.O. Hart P.E., Use of the Hough Transform to Detect Lines and Curves in Pictures, Commun. Ass. Comput. Mach., 15:11-15,(1972).

[79] MIMOSA26 User Manual, Institut Pluridisciplinaire Hubert Curien IN2P3-CNRS.

[80] J. Grosse-Knetter on behalf of the ATLAS Pixel collaboration: "The ATLAS pixel detector", NIM-A 568, 252-257 (2006).

[81] K. Arndt et al., "Silicon sensors development for the CMS pixel system", NIM-A 511 (2003).

[82] M.Deveaux, PhD thesis, Goethe Universitat, Frankfurt am Main, (2007).

[83] R. Turchetta et al., A monolithic active pixel sensor for charged particle tracking and imaging using standard VLSI CMOS technology, NIM-A **458**, Issue 3, Pages 677-689 (2001).

[84] M.Winter, CMOS Pixel Sensors for Charged Particle Tracking : Achieved Performances and Perspectives TIPP 2009, Tsukuba (12-17 March).

[85] M. Deveaux, Development of fast and radiation hard Monolithic Active Pixel Sensors (MAPS) optimized for open charm meson detection with the CBM-vertex detector, PhD thesis, Strasbourg, 2008.

[86] G. Deptuch, New Generation of Monolithic Active Pixel Sensors for Charged Parti- cle Detection / Developpement dun capteur de nouvelle generation et son electronique integr e pour les collisionneurs futurs, PhD Universit Louis Pasteur 2002.

[87] A.Dorokhov, Improved radiation tolerance of MAPS using a depleted epitaxial layer, 11th European Symposium on Semiconductor Detectors, Wildbad Kreuth (7- 11 June).

[88] C. Dritsa, M. Deveaux, Proceedings of Science, XLVIII International Winter Meeting on Nuclear Physics, in Memoriam of Ileana Iori Bormio, Italy, January 25 - 29, (2010).

[89] G. Lutz, Semiconductor Radiation Detectors, Springer (1999), ISBN 3-540-64859-3.

[90] M.Moll, Dissertaion, "Radiation damage in silicon particle detectors", Hamburg (1999).

[91] A. Akkerman, J. Barak, M.B. Chadwick, J. Levison, M.Murat, Y. Lifshitz, Updated NIEL calculations for estimating the damage induced by particles and -rays in Si and GaAs, Radiation Physics and Chemistry 62, 301-310, (2001).

[92] G.Lindstr et al, Radiation hard silicon detectors developments by the RD-48, (ROSE Collab .), NIM-A **466,** 308-326 (2001).